



**HAL**  
open science

## **NLRP3 controls ATM activation in response to DNA damage**

Mélanie Bodnar-Wachtel, Anne-Laure Huber, Julie Gorry, Sabine Hacot, Laetitia Gerossier, Baptiste Guey, Nadège Goutagny, Birke Bartosch, Elise Ballot, François Ghiringhelli, et al.

► **To cite this version:**

Mélanie Bodnar-Wachtel, Anne-Laure Huber, Julie Gorry, Sabine Hacot, Laetitia Gerossier, et al.. NLRP3 controls ATM activation in response to DNA damage. 2021. hal-03093041

**HAL Id: hal-03093041**

**<https://hal.science/hal-03093041v1>**

Preprint submitted on 5 Jan 2021

**HAL** is a multi-disciplinary open access archive for the deposit and dissemination of scientific research documents, whether they are published or not. The documents may come from teaching and research institutions in France or abroad, or from public or private research centers.

L'archive ouverte pluridisciplinaire **HAL**, est destinée au dépôt et à la diffusion de documents scientifiques de niveau recherche, publiés ou non, émanant des établissements d'enseignement et de recherche français ou étrangers, des laboratoires publics ou privés.

1 **NLRP3 controls ATM activation in response to DNA damage.**

2

3 Mélanie BODNAR-WACHTEL<sup>a,b,c,d,#</sup>, Anne-Laure HUBER<sup>a,b,c,d,#</sup>, Julie GORRY<sup>a,b,c,d</sup>, Sabine  
4 HACOT<sup>a,b,c,d</sup>, Laetitia GEROSSIER<sup>a,b,c,d</sup>, Baptiste GUEY<sup>a,b,c,d</sup>, Nadège GOUTAGNY<sup>a,b,c,d</sup>, Birke  
5 BARTOSCH<sup>a,b,c,d</sup>, Elise BALLOT<sup>e</sup>, François GHIRINGHELLI<sup>e</sup>, Bénédicte F. PY<sup>f</sup>, Yohann  
6 COUTE<sup>g</sup>, Annabelle BALLESTA<sup>h</sup>, Sylvie LANTUEJOUL<sup>d,i</sup>, Janet HALL<sup>a,b,c,d</sup>, and Virginie  
7 PETRILLI<sup>a,b,c,d\*</sup>.

8

9 <sup>a</sup> INSERM U1052, Centre de Recherche en Cancérologie de Lyon, F-69000 Lyon, France; <sup>b</sup>  
10 CNRS UMR5286, Centre de Recherche en Cancérologie de Lyon, F-69000 Lyon, France; <sup>c</sup>  
11 Université de Lyon, Université Lyon 1, F-69000 Lyon, France ; <sup>d</sup> Centre Léon Bérard, F-69008  
12 Lyon, France; <sup>e</sup> INSERM 1231, University of Burgundy, Department of Medical Oncology,  
13 France; <sup>f</sup> CIRI, Centre International de Recherche en Infectiologie, Univ Lyon, INSERM,  
14 U1111, Université Claude Bernard Lyon 1, CNRS, UMR5308, ENS de Lyon, F-69000 Lyon,  
15 France; <sup>g</sup> University Grenoble Alpes, CEA, Inserm, IRIG, BGE, 38000 Grenoble, France ; <sup>h</sup>  
16 INSERM and Paris Sud University, UMRS 935, Campus CNRS, Villejuif, F-94807, France. &  
17 Honorary position, University of Warwick, UK; <sup>i</sup> Département de Pathologie, Pôle de Biologie  
18 et de Pathologie, Centre Hospitalier Universitaire, Inserm U823, Institut A Bonniot-Université  
19 J Fourier, Grenoble, France. # contributed equally.

20 Corresponding Author: [virginie.petrilli@lyon.unicancer.fr](mailto:virginie.petrilli@lyon.unicancer.fr)

21

22 **Running title:** NLRP3 controls ATM activation

23

24 The authors declare no potential conflict of interest.

25

26 **ABSTRACT**

27

28 The DNA damage response (DDR) is essential to preserve genomic integrity and acts as a  
29 barrier to cancer. The ATM pathway orchestrates the cellular response to DNA double strand  
30 breaks (DSBs), and its attenuation is frequent during tumorigenesis. Here, we show that  
31 NLRP3, a Pattern Recognition Receptor known for its role in the inflammasome complex  
32 formation, interacts with the ATM kinase to control the early phase of DDR, independently of  
33 its inflammasome activity. NLRP3 down-regulation in human bronchial epithelial cells impairs  
34 ATM pathway activation as shown by an altered ATM substrate phosphorylation profile, and  
35 due to impaired p53 activation, confers resistance to acute genomic stress. Moreover, we found  
36 that NLRP3 is down-regulated in Non-Small Cell Lung Cancer (NSCLC) tissues and NLRP3  
37 expression is correlated with patient overall survival. NLRP3 re-expression in NSCLC cells  
38 restores appropriate ATM signaling. Our findings identify a non-immune function for NLRP3  
39 in genome integrity surveillance and strengthen the concept of a functional link between innate  
40 immunity and DNA damage sensing pathways.

41

42

43 **INTRODUCTION**

44

45 Maintenance of genome integrity is crucial for cell survival. Toxic DNA double strand breaks  
46 (DSBs) can arise from both exogenous sources, for instance exposure to ionizing radiation (IR),  
47 or endogenous sources such as DNA replication stress. If they remain unrepaired or are  
48 incorrectly repaired they represent a major risk factor for genome instability, a condition known  
49 to favor tumorigenesis. One of the key proteins that orchestrates the rapid cellular response to

50 DSBs is the Ataxia-Telangiectasia Mutated (ATM) kinase. The early molecular mechanism(s)  
51 leading to ATM activation upon DSB formation remain elusive. In resting cells, ATM is present  
52 as an inactive dimer. Once recruited to DSBs via the action of the MRE11-RAD50-NBS1  
53 (MRN) complex, ATM autophosphorylates, monomerizes and initiates a vast cascade of post-  
54 translational modifications that are essential for the DNA Damage Response (DDR) <sup>1</sup>.  
55 Phosphorylation of the histone variant H2AX on Ser139 ( $\gamma$ H2AX) is one of the earliest events  
56 in the DDR and is crucial for an efficient recruitment of DNA repair proteins to strand breaks  
57 to form Ionizing Radiation Induced Foci (IRIF) <sup>2-5</sup>. The scaffold protein MDC1 binds to  $\gamma$ H2AX  
58 and recruits more ATM to the DNA lesion thus amplifying and maintaining the DNA damage  
59 signal <sup>6,7</sup>. ATM also phosphorylates many downstream effector proteins including KAP1, p53  
60 and CHK2, which induce effector mechanisms such as the activation of cell cycle checkpoints,  
61 apoptosis or senescence <sup>8</sup>. The ATM pathway is tightly regulated and any dysregulation in these  
62 protection mechanisms facilitates the progression of cells towards malignancy.

63 NLRP3 belongs to the Nod-Like Receptor (NLR) family, a family of cytosolic Pattern  
64 Recognition Receptors (PRRs) involved in innate immunity <sup>9</sup>. Upon sensing of Pathogen-  
65 Associated Molecular Patterns (PAMPs) or Damage-Associated Molecular Patterns (DAMPs)  
66 such as nigericin or ATP, respectively, NLRP3 triggers the assembly of a multi-protein  
67 complex, the inflammasome, the function of which is to control caspase-1 activation <sup>10-12</sup>.  
68 Activated caspase-1 induces the maturation of the pro-inflammatory cytokines IL-1 $\beta$  and IL-  
69 18, and eventually pyroptosis of the cell <sup>13,14</sup>. The NLRP3 inflammasome is mostly expressed  
70 in macrophages and dendritic cells where its biological functions have been well characterized.  
71 Whether NLRP3 exerts functions unrelated to immunity remains unknown <sup>15,16</sup>. A previous  
72 study reported that in myeloid cells the NLRP3 inflammasome activity relies on the presence  
73 of ATM, suggesting a functional link between these two pathways <sup>17</sup>. Here, we investigated  
74 whether NLRP3 controls the ATM pathway. We discovered that NLRP3 binding to ATM is

75 instrumental to early ATM activation and to trigger apoptosis in response to DNA DSBs, and  
76 we report that NLRP3 expression is down-regulated in NSCLC.

77

## 78 **RESULTS**

### 79 **Loss of NLRP3 impairs $\gamma$ H2AX and P-ATM IRIF formation.**

80 To identify novel NLRP3 functions potentially linked to the regulation of the ATM pathway,  
81 we exposed HBEC3-KT cells to IR (2 Gy) and assessed the activation of the DDR pathway in  
82 the presence or absence of NLRP3. In control cells, the number of nuclear  $\gamma$ H2AX (Ser139)  
83 IRIF peaked around 1 h after IR treatment and then decreased with time as the cells underwent  
84 DNA repair (Fig. 1A and Suppl. Fig. 1A). In contrast, in the absence of NLRP3 a significantly  
85 lower number of  $\gamma$ H2AX IRIF were initially formed, and detected at all subsequent time points.  
86 This difference was greatest 1 h post IR and persisted over the time course of the study. ATM  
87 activation by DSBs relies on its monomerization which coincides with autophosphorylation on  
88 Ser1981<sup>1</sup>. Using the presence of P-ATM(Ser1981) IRIF as an endpoint for ATM activation we  
89 observed as early as 15 min post IR, fewer P-ATM foci in the absence of NLRP3, and the  
90 difference remained significant at 1 h and 5 h post-irradiation (Fig. 1B). Next, we tested whether  
91 the positive amplification loop required for optimal ATM activation was altered in the absence  
92 of NLRP3 by assessing the recruitment of MDC1 to DSBs. In siNLRP3-treated cells a  
93 decreased number of MDC1 foci were found compared with siCTL-treated cells, clearly  
94 illustrating a defect in the recruitment of MDC1 to DSBs, and, as a consequence, a defect in the  
95 ability to fully activate ATM (Fig. 1C and Suppl. Fig. 1B). 53BP1 is a DNA repair protein that  
96 also forms IRIF in response to DSBs but in an ATM-independent manner<sup>18</sup>. The levels of  
97 53BP1 foci were similar in the absence or presence of NLRP3 (Fig. 1D and Suppl. Fig. 1C),  
98 leading us to conclude that the decrease in the ability to form  $\gamma$ H2AX and P-ATM foci supports

99 a role for NLRP3 in the radiation-induced ATM DSB signaling pathway. This hypothesis was  
100 further investigated using mechanistic mathematical modeling (see Methods). Based on our  
101 experimental findings that NLRP3 KD reduced the observed number of P-ATM molecules  
102 recruited at DSBs, two hypotheses were investigated: A) NLRP3 enhances ATM activation, B)  
103 NLRP3 inhibits ATM deactivation (Suppl. Fig. 1D). Hypothesis A achieved a nearly perfect fit  
104 to data whereas hypothesis B was not able to reproduce the correct dynamics (SSR\_A=0.052,  
105 SSR\_B=0.29, Figure 1E). The model allowed to predict that the ATM activation rate in  
106 siNLRP3 conditions  $k_{IR}$  was nearly half of that in siCTL cells as the ratio  
107  $\frac{k_{IR}^{control}}{k_{IR}^{NLRP3}}$  was equal to 1.66. Thus, the model A, which best recapitulated our data, supports the  
108 notion that NLRP3 enhances ATM activation.

109

### 110 **NLRP3 is required for optimal ATM activation.**

111 To determine whether NLRP3 played a broader role in the activation of the ATM pathway, we  
112 examined the phosphorylation of ATM downstream effectors that regulate cellular outcome in  
113 response to different DSB inducers. First, we showed that the absence of NLRP3 resulted in  
114 lower levels of KAP1 Ser824 phosphorylation in response to IR (Fig. 2A). Second, we tested  
115 the response of HBEC3-KT cells to two chemotherapeutic agents known to induce DSBs,  
116 etoposide (Eto), a topoisomerase II inhibitor, and hydroxyurea (HU), that depletes cellular  
117 dNTP pools, initially inducing stalled replication forks and, following longer exposure times,  
118 fork collapse and DSBs<sup>19</sup>. Similarly, the absence of NLRP3 led to lower phosphorylation levels  
119 of KAP1 and p53 2 h to 6 h post-treatment with etoposide (Fig. 2B and C) or HU treatment  
120 (Suppl. Fig. 2A). NLRP3 down-regulation also resulted in decreased P-ATM irrespective of  
121 Eto concentrations (Suppl. Fig. 2B and C), and decreased  $\gamma$ H2AX foci formation upon Eto  
122 treatment (Suppl. Fig. 2D). These results suggest that ATM is defective in the absence of  
123 NLRP3. Previous studies reported that ATM dysfunction induces ROS production in cells<sup>17,20</sup>.

124 Consistent with these studies NLRP3-depleted cells displayed enhanced ROS content compared  
125 to control cells, which did not increase further by the addition of the ATM inhibitor KU55933  
126 (Suppl Fig. 2E). Collectively, these results strongly support the notion that NLRP3 is required  
127 for optimal ATM activation in response to DSBs.

128 We then wondered whether NLRP3 was globally required for ATM activation using a  
129 heterologous model. Murine bone marrow-derived macrophages (BMDMs) either WT or  
130 NLRP3<sup>ΔΔ</sup> treated with Eto displayed deficient ATM activation, as evidenced by reduced ATM  
131 and KAP1 phosphorylation compared to controls (Fig. 2D). As we found A549 and H292 lung  
132 cancer cells did not express NLRP3, we re-expressed NLRP3 using a doxycycline-inducible  
133 system in these NSCLC tumor cell lines, and evaluated ATM activation after IR exposure by  
134 assessing the number of P-ATM and  $\gamma$ H2AX IRIF. NLRP3 re-expression increased the levels  
135 of H2AX and ATM activating phosphorylations in both cell lines 1 h post-treatment (Fig. 3 A  
136 to D and Suppl. Fig. 3A to D). In addition, upon Eto treatment, the phosphorylation kinetics of  
137 the downstream effectors p53 and KAP1 in H292 re-expressing NLRP3 resembled those  
138 observed in non-tumoral control cells (Fig. 3E). Similar results were obtained in H520 IR-  
139 treated cells reconstituted with NLRP3 (Suppl. Fig. 3E). Thus, NLRP3 re-expression improved  
140 ATM activation.

141

#### 142 **NLRP3 controls the ATM pathway independently of its inflammasome activity.**

143 To assess if this new role for NLRP3 in DNA damage signaling is dependent on its well-known  
144 inflammasome function, caspase-1 was knocked down using siRNA. The loss of caspase-1 did  
145 not alter the level of  $\gamma$ H2AX after Eto treatment (Fig. 4A). In addition, no significant difference  
146 in the phosphorylation of H2AX was observed in HBEC3-KT cells treated with the pan-caspase  
147 inhibitor z-VAD-fmk or the caspase-1 inhibitor z-YVAD-fmk prior to HU exposure. These  
148 results would suggest that neither caspase-1 nor another caspase activity was involved in the

149 activation of the ATM pathway, thus excluding apoptosis as a source of H2AX phosphorylation  
150 (Fig. 4B). In addition, DNA damage did not activate the inflammasome as IL-1 $\beta$  release was  
151 barely detectable in cell supernatants after HU or IR treatments, nor could we detect cleaved  
152 caspase-1 after Eto treatment (Fig. 4C, D, and E). Thus, DNA DSBs do not activate the catalytic  
153 activity of the inflammasome.

154

### 155 **NLRP3 forms a complex with ATM.**

156 To determine how NLRP3 regulates ATM activity, we tested whether these two proteins could  
157 interact with each other. In HeLa cells, that do not express endogenous NLRP3, co-  
158 immunoprecipitation of Flag-ATM pulled down mCherry-NLRP3 (Fig. 5A). Moreover,  
159 Flag-NLRP3 co-immunoprecipitated endogenous ATM (Fig. 5B)<sup>21</sup>. Eto treatment dissociated  
160 the interaction, suggesting that ATM and NLRP3 formed a complex under basal cell condition  
161 (Fig. 5B). We then mapped the NLRP3 domain involved in its binding to ATM. We showed  
162 that ATM interacted with the NACHT (domain present in neuronal apoptosis inhibitor protein,  
163 the major histocompatibility complex class II transactivator, HET-E and TPI), and the LRR  
164 (Leucin Rich Repeats) domains but not with the PYD (Pyrin) domain, which is known to  
165 mediate homotypic interactions involved in inflammasome formation (Fig. 5C)<sup>10</sup>. NEK7 was  
166 used as a positive assay control, as it is a known partner of NLRP3 (Fig. 5C). We next  
167 investigated whether NLRP3 was able to translocate to the nucleus. Cell fractionation  
168 experiments revealed that endogenous NLRP3 was present in both the cytosolic and nuclear  
169 fractions (Suppl. Fig. 4A) supporting earlier findings<sup>22</sup>. Interestingly, IF labeling of NLRP3  
170 domains revealed nuclear localizations for the NACHT and the LRR domains, and a cytosolic  
171 localization for the PYD domain, which self-oligomerized as previously described for ASC  
172 PYD (Suppl. Fig. 4B)<sup>23</sup>. Using this technique, short and full length (FL) NLRP3 were weakly  
173 detected in the nucleus (Suppl. Fig. 4B). However, live-imaging of mCherry-NLRP3 revealed

174 its presence in the cell nucleus (Suppl. Fig. 4C). Consistently, co-immunoprecipitation  
175 experiments revealed that NLRP3 bound to IPO5 and XPO2 two proteins involved in nuclear  
176 import and export, respectively, which we identified by mass spectrometry (Fig. 5C)<sup>24,25</sup>.  
177 Using Proximity Ligation Assay (PLA), we also showed in HeLa cells that Flag-NLRP3 and  
178 endogenous ATM formed a complex (Suppl. Fig. 4D). Importantly, we validated that  
179 endogenous ATM and NLRP3 interacted in HBEC3-KT cells, and that the complex was  
180 dissociated upon Eto treatment (Fig. 5D). We also observed after DNA damage that a smaller  
181 fraction of ATM was detected by IF in the nucleus of NLRP3-depleted cells compared with  
182 control cells (Suppl. Fig. 5A, B). Collectively, these results establish that under homeostatic  
183 conditions NLRP3 forms a complex with ATM, which dissociates upon DSB formation.

184

#### 185 **NLRP3-depleted cells are resistant to genotoxic stress-induced cell death.**

186 Because ATM activity controls cell fate decisions in response to genotoxic stress, we next  
187 monitored cell death in response to Eto treatment. In NLRP3-depleted HBEC3-KT cells, less  
188 caspase-3/7 activity was detected compared with control conditions, and an increase in the  
189 number of viable cells was observed (Fig. 6A and B). These results suggest that decreased  
190 NLRP3 expression protects cells from etoposide-induced apoptosis. Indeed, the induction of  
191 *PUMA* and *NOXA/PMAIP1*, two p53 apoptosis effector genes, was significantly reduced in the  
192 absence of NLRP3 compared to control cells (Fig. 6C and D)<sup>26,27</sup>. This response was specific  
193 to genotoxic stress as the induction of apoptosis via death receptor activation using a  
194 combination of TRAIL and MG132 did not result in impaired apoptosis in cells depleted for  
195 NLRP3 (Suppl. Fig. 6A and B).

196

#### 197 **NLRP3 is down-regulated in NSCLC.**

198 GWAS studies reported that *NLRP3* is frequently mutated in NSCLC, but we found that A549  
199 and H292 cells, isolated from NSCLC patients, do not express NLRP3. To extend this  
200 observation, we assembled a panel of NSCLC cell lines, and included 3 HBEC3-KT cell lines  
201 for comparison<sup>28</sup>. Paradoxically, in most of the NSCLC cell lines, including cell lines reported  
202 to carry NLRP3 mutations, the NLRP3 protein was barely detectable (Fig. 7A and Suppl. Fig.  
203 7A), and very low levels of *NLRP3* mRNA were observed by Q-RT-PCR in comparison with  
204 HBEC3-KT cells (Fig. 7B). Among the 3 HBEC3-KT lines, the HBEC3-ET cells did not  
205 express NLRP3, and those cells displayed properties of malignant transformation since they  
206 were able to grow in an anchorage-independent manner (Suppl Fig. 7B). These results suggest  
207 that NLRP3 expression is down-regulated in malignant cells. To validate these observations,  
208 we obtained a set of RNA samples from a cohort of patients with primary NSCLC and from  
209 adjacent normal lung tissues. As shown in Fig. 7C, *NLRP3* mRNA was detectable in normal  
210 lung tissues, while it was significantly down-regulated in NSCLC tissues. Finally, analysis of  
211 TCGA data showed that high NLRP3 expression in lung adenocarcinoma (LUAD) was  
212 associated with better overall survival and better progression-free interval (Fig. 7D and E).  
213 Altogether, these results suggest a down-regulation of NLRP3 in NSCLC, and a positive  
214 correlation in LUAD between NLRP3 levels and patient outcome.

215

216

## 217 **Discussion**

218 Functional links between innate immunity and DNA damage sensing pathways have been  
219 described. For instance, ATM was recently shown to be required in macrophages for optimal  
220 NLRP3 and NLRC4 inflammasome functions because its inactivation altered the ROS balance  
221 and therefore impaired inflammasome assembly<sup>17</sup>. It was also suggested that DDR proteins  
222 such as RAD50 or BRCA1 are involved in the sensing of nucleic acids from viral pathogens in

223 the cytosol <sup>29,30</sup>. However, little is known about the contribution of PRRs to the sensing of stress  
224 like DNA damage. Here, we demonstrate that NLRP3 is crucial to reach optimal ATM  
225 activation. Under homeostatic conditions, our PLA data showed that NLRP3 forms a complex  
226 with ATM in the cytosol, suggesting that NLRP3 binds to the inactive ATM dimer. ATM has  
227 already been reported to be found in the cell cytosol <sup>20,31</sup>. Upon DNA DSB formation, the  
228 complex dissociates to allow ATM relocalization and monomerization onto DNA breaks. In  
229 the absence of NLRP3, decreased levels of P-ATMSer1981 foci were observed herein, together  
230 with a decreased nuclear ATM pool. These observations suggest that NLRP3 may control either  
231 ATM translocation to the nucleus or ATM monomerization. Consequently, the formation of  
232  $\gamma$ H2AX and MDC1 IRIF, which are both essential for the positive ATM amplification loop  
233 signaling, were also impaired in NLRP3 KD cells <sup>6</sup>. This led to a less active ATM as illustrated  
234 by the reduced phosphorylation of its substrates KAP-1 and p53, and, importantly, cells became  
235 more resistant to apoptosis.

236 No caspase-1 activation and no significant IL-1 $\beta$  production was detected upon DNA DSB  
237 induction. Our findings contrast with those of R. Flavell's group, who demonstrated in mouse  
238 models that the severe damage caused to the gastrointestinal tract and the hematopoietic system  
239 in response to whole body  $\gamma$ -irradiation are due to the activation of the AIM2 inflammasome by  
240 DSBs, which cause massive cell death by caspase-1-dependent pyroptosis in these fast  
241 renewing tissues. These observations would suggest that tissue and species-specific differences  
242 may exist that clearly warrant further investigation <sup>32</sup>.

243 Using different approaches which included restoring NLRP3 expression in NSCLC cell lines  
244 displaying low levels of inflammasome proteins, we identified a novel non-inflammasome  
245 function for NLRP3 in the DNA damage pathway. This previously unappreciated role for  
246 NLRP3 in the ATM pathway may be due to the fact that many common cellular models used  
247 in laboratories do not express NLRP3 (e.g. MEF, HeLa, 293, A549). Altogether, our results

248 highlight that NLRP3 is not only a major player in innate immunity but is also a key factor  
249 involved in the preservation of genome integrity through the modulation of the ATM signaling  
250 pathway in response to DSBs.

251 The DDR is known to be a barrier to cancer in the early phases of tumorigenesis<sup>33,34</sup>. *TP53* is  
252 frequently mutated in cancer, and the ATM pathway is down-regulated in many solid tumors:  
253 11% of NSCLC carry somatic mutations in *ATM* and 41% of lung adenocarcinoma have  
254 reduced ATM protein expression<sup>35-38</sup>. Although, several cancer genomic studies have reported  
255 that *NLRP3* is frequently mutated in NSCLC, our data actually suggest that in NSCLC primary  
256 human tissues and cell lines its expression is significantly lower compared to normal tissue.  
257 This down-regulation of *NLRP3* expression during malignant transformation may represent an  
258 additional mechanism to attenuate ATM and p53 signaling pathways, allowing cells to survive  
259 genotoxic stress, despite the presence of genome alterations. Thus, the loss of NLRP3, and the  
260 subsequent impairment of the ATM pathway could be an event allowing cells to progress  
261 towards malignancy.

262

263

## 264 **MATERIALS AND METHODS**

### 265 *Cell culture*

266 HBEC3-KT, HCC15, HCC366, HCC4017 and HCC461 were obtained from J. Minna, NCI-  
267 H1703 (H1703), NCI-H292 (H292), NCI-H520 (H520), NCI-H661 (H661), NCI-H358 (H358),  
268 NCI-H1792 (H1792), NCI-H441 (H441) and SK-MES-1 from ATCC, and A549 from the PHE  
269 culture collection. HBEC3-KT cells were cultured in Keratinocyte-Serum Free Medium  
270 (Invitrogen) supplemented with 12.5 mg of Bovine Pituitary Extract (Invitrogen) and 100 ng of  
271 epidermal growth factor (Invitrogen). H1792, A549, HCC15, HCC366, HCC4017, HCC461  
272 and H441 were cultured in RPMI medium, supplemented with 10% Fetal Bovine Serum (FBS)

273 and 1% penicillin/streptomycin, H1703, H292, H520, H358, H661 in RPMI, 10% FBS, 1 mM  
274 sodium pyruvate, 1 mM HEPES and 1% penicillin/streptomycin and SK-MES-1 in RPMI, 10%  
275 FBS, 1 mM sodium pyruvate, 1 mM non-essential amino acids and 1 % penicillin/streptomycin  
276 (Invitrogen). *NLRP3* mutated cell lines are H661, H358, HCC15, HCC366 and HCC4017.  
277 HeLa cells were cultured in DMEM 4.5 g/L of glucose, 10% FCS and 1%  
278 penicillin/streptomycin. Treated cells received Etoposide (TEVA santé), HU (Sigma) or  $\gamma$ -ray  
279 treatment 24 h post-transfection. For inflammasome activation, cells were primed overnight  
280 with 10  $\mu$ g/mL poly(I:C) (Invivogen) and treated with nigericin (10  $\mu$ M, 6 h), or ATP (5 mM,  
281 30 min) (SIGMA). IL-1 $\beta$  ELISA was purchased from BD. Z-VAD-fmk and z-YVAD-fmk were  
282 from Enzo Life Science.

283

#### 284 *Mice*

285 The *NLRP3* flox mice were generated by the “clinique de la souris” Strasbourg. The exon 4  
286 was flanked by 2 Lox-P sites in C57BL6 background. *NLRP3*<sup>flox/flox</sup> mice were bred with  
287 Rosa26-Cre-ERT2 mice. Bone marrow-derived macrophages were generated as previously  
288 described <sup>39</sup> from +/+; Cre-ERT2 and Flox/Flox; Cre-ERT2 adult mice. To inactivate *Nlrp3*  
289 (*Nlrp3* <sup>$\Delta\Delta$</sup> ), 4OHT (SIGMA) was added at the concentration of 0.5  $\mu$ M from day 2 to day 7 of  
290 differentiation in both genotypes for control. BMDM were treated with 100  $\mu$ M Eto as  
291 indicated.

292

#### 293 *Cell transfection*

294 HBEC3-KT were seeded at 1.5x10<sup>5</sup> cells per well in 6-well plates and were transfected with  
295 non-targeting siRNA (SMART pool Non-targeting siRNA, Dharmacon) or *NLRP3* siRNA  
296 (SMARTpool, Dharmacon) using HiPerfect transfection reagent (Qiagen) or INTERFERin  
297 (Polyplus transfection) following manufacturer’s instructions. HeLa cells were transfected with

298 Lipofetamin2000™ (Invitrogen). H292 cells were transfected using PEI method. Vectors used  
 299 pCR3-Flag-NLRP3 (FL, SHORT, PYD, NACHT, LRR), pcDNA3.1-Flag-His-ATM (Addgene  
 300 31985), pcDNA3.1-mCherry-NLRP3. shRNA were from Genecopoeia, hygromycin selection,  
 301 *NLRP3*: forward: 5'-TAATACGACTCACTATAGGG-3' Reverse: 5'-  
 302 CTGGAATAGCTCAGAGGC-3'; control Forward: 5'-TAATACGACTCACTATAGGG-3'  
 303 Reverse: 5'-CTGGAATAGCTCAGAGGC-3'.

#### 304 *Irradiation*

305 Cells were irradiated using a 6-MeV  $\gamma$ -ray clinical irradiator (SL 15 Phillips) at the Léon Bérard  
 306 Cancer Centre (Lyon, France) with a dose rate of 6 Gy.min<sup>-1</sup> to obtain the required dose.

307

#### 308 *ROS measurement*

309 For intracellular ROS staining, HBEC3-KT cells were incubated with 1  $\mu$ M of 2',7'-  
 310 dichlorofluorescein diacetate (CM-H2DCFDA; Invitrogen) for 30 min at 37°C. For a positive  
 311 control, cells were pretreated with 5  $\mu$ M of ATM inhibitor (ATMi) (KU55933; Selleckchem)  
 312 for 5 h prior to staining. Stained cells were collected and analyzed on a BD FACSCalibur, and  
 313 data were analyzed using the FlowJo software.

314

#### 315 *Mathematical modeling*

316 ATM dynamics was modeled using the following ordinary differential equation:

$$317 \quad \frac{dA}{dt} = k_{IR} \mathbb{1}_{t \in [IR \text{ exposure}]} - k_{inact} A$$

318 where A is the concentration of activated ATM molecules (expressed in number of foci/cell),  
 319  $k_{IR}$  is the activation rate (in number of foci/cell. h<sup>-1</sup>), only present during irradiation, and  $k_{inact}$   
 320 is the inactivation rate (in h<sup>-1</sup>). A was set at zero at t<sub>0</sub>. This model assumed that ATM molecules  
 321 were in excess compared to the activated proportion.

322 The model is fitted to experimental data by estimating the optimal values for  $k_{IR}$  and  $k_{inact}$  for  
323 each condition- siCTL or siNLRP3- using a weighted least-square approach<sup>40</sup>. For hypothesis  
324 A, i.e. NLRP3 enhances ATM activation,  $k_{IR}$  is assumed to be different for both conditions  
325 whereas  $k_{inact}$  is taken identical. For hypothesis B, i.e. NLRP3 inhibits ATM deactivation,  
326  $k_{inact}$  is assumed to vary between siCTL and siNLRP3 conditions and  $k_{IR}$  is assumed to remain  
327 identical. All computations were done in Matlab (Mathworks, USA).

328

### 329 *Generation of NLRP3 stably expressing cells*

330 The human *NLRP3* cDNA was inserted into the lentiviral vector pSLIKneo (addgene)  
331 containing a TET-ON promoter using the Gateway recombination system (Invitrogen).  
332 Sequences of the Gateway shuttle vectors are available upon request. Empty pSLIK vector  
333 (without the ccdB containing Gateway recombination cassette) was produced by partial  
334 digestion with Xba1 and Xho1 followed by religation. Viral particles were produced by  
335 transfecting HEK293T cells with the lentiviral vectors and a second generation packaging  
336 system. NCI-H292, NCI-H520 and A549 cells were either transduced with the empty pSLIK  
337 control vector or the NLRP3 containing vector. NLRP3 expression was induced by adding 0.5  
338  $\mu\text{g/mL}$  doxycycline (Takara Bio) to the cell culture medium.

339

### 340 *Western blotting*

341 Cells were washed with PBS and detached by trypsinization. Cell pellets were lysed in Laemmli  
342 buffer x2 (Tris HCl 0.5 M pH 6.8; 0.5 M DTT; 0.5% SDS) and protein concentrations were  
343 determined using the Bradford reagent (Biorad). Protein extracts were separated on SDS-PAGE  
344 (8 % or 15 % or 4-15% gradient (vol/vol)) gels. Gels were transferred onto nitrocellulose  
345 membranes (GE HealthCare and Biorad) for immunoblotting with the following antibodies:  
346 anti-NLRP3 (Cryo-2, 1:1000) and anti-caspase-1 (Bally-1, 1:1000) from Adipogen, anti-ASC

347 (1:2000) from ENZO Life Science, anti- $\gamma$ H2AX (JBW301, 1:1000), anti-P-Ser15-p53 (1:1000)  
348 and anti-ATM Ser1981 (10H11.E12, 1:200) were from Millipore. Anti-P-KAP1Ser824  
349 (1:1000), anti-KAP1 (1:1000) and anti-Nek7 (A302-684A) from Bethyl Laboratories, anti-p53  
350 (clone DO7 1:2000) and anti-NOXA (114C307, 1:1000) from Santa Cruz, anti-ATM  
351 (#ab32420, 1/1000) from Abcam, anti-Flag (F7425 1/5000) from Sigma, anti-XPO2  
352 (GTX102005 1/1000) and anti-IPO5 (GTX114515 1/1000) from Genetex and anti-actin (C4,  
353 1:100,000) from MP Biomedical.

354 The Fiji and ImageLab programs were used for densitometric analysis of immunoblots, and the  
355 quantified results were normalized as indicated in the figure legends.

356

#### 357 *Cell fractionation*

358 HBEC3-KT were fractionated by adapting the method described by Hacot *et al.*<sup>41</sup>. The MgCl<sub>2</sub>  
359 concentration used for the hypotonic buffer was 0.75 mM. Equal amounts of proteins were run  
360 by SDS-PAGE.

361

#### 362 *Immunofluorescence*

363 Cells were plated onto sterile glass coverslips and fixed with PBS-PFA 4% (wt/vol) for 15 min  
364 at room temperature (RT) and washed twice in PBS. Cells were permeabilized with lysis buffer  
365 (sucrose 300 mM, MgCl<sub>2</sub> 3 mM, Tris pH 7.0 20 mM, NaCl 50 mM, Triton X-100 0.5%) for 3-  
366 5 min at RT under slow agitation. The following antibodies were diluted in PBS-BSA 4% and  
367 applied to the coverslips for 40 min at 37°C: anti- $\gamma$ H2AX (JBW301, 1:800), P-ATM Ser1981  
368 (10H11.E12, 1:200), and 53BP1 (1:500) from Millipore, and anti-MDC1 (1:200) from AbCam.  
369 For NLRP3 labeling, cells were fixed with PBS-PFA 4% (wt/vol) for 15 min at RT, washed  
370 twice in PBS and permeabilized with 1% triton X100. Anti-flag was diluted in saturation buffer  
371 (PBS, 1% BSA; NaCl 0.02%; Tween 20 0.5%; SVF 3%) and incubated on cells for 1 h. Cells

372 were then incubated with Alexa-Fluor 488-conjugated anti-mouse or Alexa-Fluor 555-  
373 conjugated anti-rabbit (1:800; Life Technologies) for 20 min at 37°C and in Hoechst (500  
374 ng/mL in PBS) for 10 min at RT. Fluorescence microscopy pictures were taken using a Nikon  
375 Eclipse Ni-E microscope, and confocal Zeiss LSM 780. The Fiji program was used to analyze  
376 fluorescence intensity.

377

### 378 *Live imaging*

379 mCherry-NLRP3 transfected H292 were imaged using a confocal spinning disk inverted  
380 microscope (Leica, Yokogawa). Vital Hoechst was used at 0.5  $\mu$ g/mL. The Fiji program was  
381 used to analyze fluorescence intensity.

382

### 383 *Co-immunoprecipitation*

384 HeLa cells were transfected using Lipofectamin2000<sup>TM</sup> (Invitrogen) according to  
385 manufacturer's protocol, and lysed in the following buffer: Tris HCl 100 mM pH 8.0, 10 mM  
386 MgCl<sub>2</sub>, 90 mM NaCl, 0.1% Triton X-100, Complete® tablet (Roche). Immunoprecipitation was  
387 performed using M2-agarose beads (A2220 Sigma) overnight at 4°C.

388

### 389 *Proximity Ligation Assay*

390 HBECT3-KT and HeLa cells were seeded onto glass coverslips and processed as described by  
391 the manufacturer's protocol (Duolink® PLA Technology, Sigma). Antibodies used NLRP3  
392 1/500 (ABF23, Millipore), ATM 1/500 (2C1, Abcam). Quantification was carried out using the  
393 macro published by Poulard et al <sup>42</sup>.

394

### 395 *IL-1 $\beta$ Luminex Assay*

396 IL-1 $\beta$  levels in cell supernatants were analyzed using the Magnetic Luminex Screening Assay  
 397 according to the manufacturer's protocol (R&DSystems). The samples were read using the  
 398 Bioplex-200 from BioRad.

399

#### 400 *Quantitative reverse transcription PCR*

401 Cells were washed and detached by trypsinization. RNA was extracted using NucleoSpin<sup>®</sup> RNA  
 402 kit (Macherey Nagel). Five hundred nanograms to one microgram of RNA were reverse  
 403 transcribed using SuperScript II reverse transcriptase and oligo(dT) primers (Life technologies)  
 404 and RNAsin (Promega). cDNAs were quantified by real-time PCR using a SYBR<sup>®</sup> Green PCR  
 405 Master Mix (Applied Biosystems) on a ABI Prism<sup>®</sup> 7000 (Applied Biosystems) or CFX  
 406 Connect Real-Time system (BioRad). Sequences of the primers NLRP3 Forward 5'-  
 407 GAAGAAAGATTACCGTAAGAAGTACAGAAA; Reverse 5'-  
 408 CGTTTGTTGAGGCTCACACTCT; ESD 5'-TTAGATGGACAGTTAC TCCCTGATAA;  
 409 Reverse 5'-GGTTGCAATGAAGTAGTAGCTATGAT; HPRT1 Forward 5'-  
 410 CATTATGCTGAGGATTTGGAAAGG; Reverse 5'-TGTAGCCCTCTGTGTGCTCAAG;  
 411 CBP Forward 5'-CGGCTGTTTAACTTCGCTTC; Reverse 5'-  
 412 CACACGCCAAGAAACAGTGA. NOXA Forward 5'-GGAGATGCCTGGGAAGAAG;  
 413 Reverse 5'-CCTGAGTTGAGTAGCACACTCG; PUMA Forward 5'-  
 414 CCTGGAGGGTCCTGTACAATCTCAT; Reverse 5'-  
 415 GTATGCTACATGGTGCAGAGAAAG; ACTIN Forward 5'-  
 416 AGCACTGTGTTGGCGTACAG; Reverse 5'-TCCCTGGAGAAGAGCTACGA.

417 NLRP3 mRNA amounts in different NSCLC cell lines were normalized against *ESD* (Fig. 1B)  
 418 or in human samples on *CPB* and *HPRT1* (Fig. 1D) mRNA levels or in HBEC-KT on *HPRT1*  
 419 (Fig. 5C).

420

421 *Caspase-3/7 assay*

422 Cells were cultured in 96-well plates and treated with 50  $\mu$ M of Etoposide for 12 h or with 200  
423 ng/mL Trail (Peprotech) and 1 mM MG132 (Sigma). Caspase 3/7 activity was assessed using  
424 the Caspase-Glo 3/7 assay reagent (Promega) following the manufacturer's instructions. The  
425 luminescence was measured using a TECAN Infinite M200PRO luminometer microplate  
426 reader. To normalize the results, a second plate was stained with crystal violet and analyzed as  
427 described in the *crystal violet cytotoxicity assay* below.

428

429 *Crystal Violet cytotoxicity assay*

430 Cells were stained with 0.5% crystal violet (Sigma-Aldrich Corp.) in 30% methanol for 20  
431 minutes at room temperature. Cells were lysed in a 1% SDS (Sigma-Aldrich Corp.) solution.  
432 The absorbance of the solution was measured using a TECAN Infinite M200PRO microplate  
433 reader at a wavelength of 595 nm.

434

435 *Tissues from NSCLC patients*

436 Frozen lung tumor tissues from non-treated patients were obtained from the Biological  
437 Resource Centre in Grenoble (Centre de Ressources biologiques de Grenoble) n°BB-0033-  
438 00069 and in accordance with the ethical laws. RNA was extracted from regions containing  
439 mainly malignant cells using Allprep RNA/DNA kit from Qiagen.

440

441 *TCGA data analysis*

442 RNAseqV2 data of lung adenocarcinoma (LUAD) and corresponding clinical data were  
443 downloaded from The Cancer Genome Atlas TCGA data portal. Cox regression model was  
444 used to estimate hazard ratio (HR) and 95% confidence intervals (CIs) for overall survival (OS)  
445 and progression-free interval (PFI). Survival curve was estimated by the Kaplan–Meier method.

446 Optimal cutoff for NLRP3 expression was chosen based on a maximally selected rank statistic  
447 <sup>43</sup>.

448

449

450

451 *Statistical analysis*

452 Statistical analysis of the experimental data was performed using Graphpad. Unpaired group  
453 comparisons were done using two-tailed Student t-test for most figures, Mann-Whitney test for  
454 Figure 5A and B and multiple comparisons for two-way ANOVA for Figure 5C.

455

456 **Acknowledgements:** We thank John Minna for sharing the HBEC3-KT and NSCLC cells, Dr  
457 Foray's team and Marine Malfroy for technical help and Agnès Tissier and Pascale Bertrand  
458 for helpful discussions. We thank Christophe Vanbelle and Christophe Chamot for their  
459 assistance on confocal microscope image acquisition. M.B. was supported by the ANRT, V.P.  
460 by the plan Cancer, Ligue Contre le Cancer Comité de l'Ain, the ARC foundation, and the  
461 Fondation pour la Recherche Médicale DEQ20170336744, A.L.H. by the ARC foundation and  
462 a Marie Skodolvska-Curie grant, N.G. was supported by the CLARA, and B.G. by the ARC  
463 foundation. B.P. was supported by the ERC.

464

465 **Author contributions:** M.B.W., A.L.H., J.G., S.H., J.H. and V.P. designed and analyzed  
466 experiments. M.B.W., A.L.H., J.G., B.G., S.H., Y.C., L.G. and V.P. performed experiments.  
467 F.G., B.B., B.P., S.L., B.P. and N.G. provided reagents. M.B.W., A.L.H., J.G., S.H., J.H. and  
468 V.P. contributed to the manuscript writing and figure constructions.

469

470 Competing interests: the authors declare no financial competing interest.

471

472

473 **REFERENCES**

- 474 1 Bakkenist CJ, Kastan MB. DNA damage activates ATM through intermolecular  
475 autophosphorylation and dimer dissociation. *Nature* 2003; **421**: 499–506.
- 476 2 Celeste A, Petersen S, Romanienko PJ, Fernandez-Capetillo O, Chen HT, Sedelnikova  
477 O a *et al.* Genomic instability in mice lacking histone H2AX. *Science* 2002; **296**: 922–  
478 927.
- 479 3 Xie A, Puget N, Shim I, Odate S, Jarzyna I, Bassing CH *et al.* Control of sister  
480 chromatid recombination by histone H2AX. *Mol Cell* 2004; **16**: 1017–25.
- 481 4 Burma S, Chen BP, Murphy M, Kurimasa A, Chen DJ. ATM phosphorylates histone  
482 H2AX in response to DNA double-strand breaks. *J Biol Chem* 2001.  
483 doi:10.1074/jbc.C100466200.
- 484 5 Paull TT, Rogakou EP, Yamazaki V, Kirchgessner CU, Gellert M, Bonner WM. A  
485 critical role for histone H2AX in recruitment of repair factors to nuclear foci after DNA  
486 damage. *Curr Biol* 2000; **10**: 886–895.
- 487 6 Lou Z, Minter-Dykhouse K, Franco S, Gostissa M, Rivera MA, Celeste A *et al.* MDC1  
488 maintains genomic stability by participating in the amplification of ATM-dependent  
489 DNA damage signals. *Mol Cell* 2006; **21**: 187–200.
- 490 7 Stucki M, Clapperton J a., Mohammad D, Yaffe MB, Smerdon SJ, Jackson SP. MDC1  
491 Directly Binds Phosphorylated Histone H2AX to Regulate Cellular Responses to DNA  
492 Double-Strand Breaks. *Cell* 2005; **123**: 1213–1226.
- 493 8 Smith J, Tho LM, Xu N, Gillespie DA. The ATM-Chk2 and ATR-Chk1 pathways in  
494 DNA damage signaling and cancer. *Adv Cancer Res* 2010; **108**: 73–112.

- 495 9 Martinon F, Tschopp J. NLRs join TLRs as innate sensors of pathogens. *Trends*  
496 *Immunol* 2005; **26**: 447–454.
- 497 10 Schroder K, Tschopp J. The inflammasomes. *Cell* 2010; **140**: 821–32.
- 498 11 Mariathasan S, Weiss DS, Newton K, McBride J, O'Rourke K, Roose-Girma M *et al.*  
499 Cryopyrin activates the inflammasome in response to toxins and ATP. *Nature* 2006;  
500 **440**: 228–32.
- 501 12 Pétrilli V, Dostert C, Muruve D a DA, Tschopp J, Petrilli V, Dostert C *et al.* The  
502 inflammasome: a danger sensing complex triggering innate immunity. *Curr Opin*  
503 *Immunol* 2007; **19**: 615–22.
- 504 13 Agostini L, Martinon F, Burns K, McDermott MF, Hawkins PN, Tschopp J. NALP3  
505 forms an IL-1beta-processing inflammasome with increased activity in Muckle-Wells  
506 autoinflammatory disorder. *Immunity* 2004; **20**: 319–325.
- 507 14 Mariathasan S, Monack DM. Inflammasome adaptors and sensors: intracellular  
508 regulators of infection and inflammation. *Nat Rev Immunol* 2007; **7**: 31–40.
- 509 15 Guarda G, Zenger M, Yazdi AS, Schroder K, Ferrero I, Menu P *et al.* Differential  
510 expression of NLRP3 among hematopoietic cells. *J Immunol* 2011; **186**: 2529–2534.
- 511 16 Wang W, Wang X, Chun J, Vilaysane A, Clark S, French G *et al.* Inflammasome-  
512 Independent NLRP3 Augments TGF- $\beta$  Signaling in Kidney Epithelium. *J Immunol*  
513 2013; **190**: 1239–49.
- 514 17 Erttmann SF, Härtlova A, Sloniecka M, Raffi FAM, Hosseinzadeh A, Edgren T *et al.*  
515 Loss of the DNA Damage Repair Kinase ATM Impairs Inflammasome-Dependent  
516 Anti-Bacterial Innate Immunity. *Immunity* 2016; **45**: 106–118.
- 517 18 DiTullio RA, Mochan TA, Venere M, Bartkova J, Sehested M, Bartek J *et al.* 53BP1  
518 functions in an ATM-dependent checkpoint pathway that is constitutively activated in

- 519 human cancer. *Nat Cell Biol* 2002; **4**: 998–1002.
- 520 19 Saintigny Y, Delacôte F, Varès G, Petitot F, Lambert S, Averbek D *et al.*  
521 Characterization of homologous recombination induced by replication inhibition in  
522 mammalian cells. *EMBO J* 2001; **20**: 3861–3870.
- 523 20 Alexander A, Cai S-L, Kim J, Nanez A, Sahin M, MacLean KH *et al.* ATM signals to  
524 TSC2 in the cytoplasm to regulate mTORC1 in response to ROS. *Proc Natl Acad Sci U*  
525 *S A* 2010; **107**: 4153–8.
- 526 21 Shi H, Wang Y, Li X, Zhan X, Tang M, Fina M *et al.* NLRP3 activation and mitosis  
527 are mutually exclusive events coordinated by NEK7, a new inflammasome component.  
528 *Nat Immunol* 2015; **advance on**. doi:10.1038/ni.3333.
- 529 22 Bruchard M, Rebé C, Derangère V, Togbé D, Ryffel B, Boidot R *et al.* The receptor  
530 NLRP3 is a transcriptional regulator of TH2 differentiation. *Nat Immunol* 2015; **16**:  
531 859–70.
- 532 23 Lu A, Magupalli VG, Ruan J, Yin Q, Atianand MK, Vos MR *et al.* Unified  
533 polymerization mechanism for the assembly of asc-dependent inflammasomes. *Cell*  
534 2014; **156**: 1193–1206.
- 535 24 Soniat M, Chook YM. Nuclear localization signals for four distinct karyopherin- $\beta$   
536 nuclear import systems. *Biochem J* 2015; **468**: 353–362.
- 537 25 Güttler T, Görlich D. Ran-dependent nuclear export mediators: a structural perspective.  
538 *EMBO J* 2011; **30**: 3457–3474.
- 539 26 Shibue T, Takeda K, Oda E, Tanaka H, Murasawa H, Takaoka A *et al.* Integral role of  
540 Noxa in p53-mediated apoptotic response. *Genes Dev* 2003. doi:10.1101/gad.1103603.
- 541 27 Nakano K, Vousden KH. PUMA, a novel proapoptotic gene, is induced by p53. *Mol*  
542 *Cell* 2001. doi:10.1016/S1097-2765(01)00214-3.

- 543 28 Ramirez RD, Sheridan S, Girard L, Sato M, Kim Y, Pollack J *et al.* Immortalization of  
544 human bronchial epithelial cells in the absence of viral oncoproteins. *Cancer Res* 2004;  
545 **64**: 9027–34.
- 546 29 Roth S, Rottach A, Lotz-Havla AS, Laux V, Muschwackh A, Gersting SW *et al.*  
547 Rad50-CARD9 interactions link cytosolic DNA sensing to IL-1 $\beta$  production. *Nat*  
548 *Immunol* 2014; **15**: 538–45.
- 549 30 Dutta D, Dutta S, Veetil MV, Roy A, Ansari MA, Iqbal J *et al.* BRCA1 Regulates  
550 IFI16 Mediated Nuclear Innate Sensing of Herpes Viral DNA and Subsequent  
551 Induction of the Innate Inflammasome and Interferon- $\beta$  Responses. *PLoS Pathog* 2015;  
552 **11**: e1005030.
- 553 31 Fiévet A, Bellanger D, Rieunier G, Dubois d’Enghien C, Sophie J, Calvas P *et al.*  
554 Functional classification of ATM variants in ataxia-telangiectasia patients. *Hum Mutat*  
555 2019. doi:10.1002/humu.23778.
- 556 32 Hu S, Peng L, Kwak Y-TT, Tekippe EM, Pasare C, Malter JS *et al.* The DNA Sensor  
557 AIM2 Maintains Intestinal Homeostasis via Regulation of Epithelial Antimicrobial  
558 Host Defense. *Cell Rep.* 2015; **13**: 1922–36.
- 559 33 Bartkova J, Horejsí Z, Koed K, Krämer A, Tort F, Zieger K *et al.* DNA damage  
560 response as a candidate anti-cancer barrier in early human tumorigenesis. *Nature* 2005;  
561 **434**: 864–870.
- 562 34 Lantuejoul S, Raynaud C, Salameire D, Gazzeri S, Moro-Sibilot D, Soria J-C *et al.*  
563 Telomere maintenance and DNA damage responses during lung carcinogenesis. *Clin*  
564 *Cancer Res* 2010; **16**: 2979–88.
- 565 35 Ding L, Getz G, Wheeler DA, Mardis ER, McLellan MD, Cibulskis K *et al.* Somatic  
566 mutations affect key pathways in lung adenocarcinoma. *Nature* 2008; **455**: 1069–1075.

- 567 36 Hammerman PS, Hayes DN, Wilkerson MD, Schultz N, Bose R, Chu AALA *et al.*  
568 Comprehensive genomic characterization of squamous cell lung cancers. *Nature* 2012;  
569 **489**: 519–25.
- 570 37 Imielinski M, Berger AH, Hammerman PS, Hernandez B, Pugh TJ, Hodis E *et al.*  
571 Mapping the hallmarks of lung adenocarcinoma with massively parallel sequencing.  
572 *Cell* 2012; **150**: 1107–1120.
- 573 38 Villaruz LC, Jones H, Dacic S, Abberbock S, Kurland BF, Stabile LP *et al.* ATM  
574 protein is deficient in over 40% of lung adenocarcinomas. *Oncotarget* 2016.  
575 doi:10.18632/oncotarget.9757.
- 576 39 Guey B, Bodnar M, Manié SNSN, Tardivel A, Petrilli V. Caspase-1 autoproteolysis is  
577 differentially required for NLRP1b and NLRP3 inflammasome function. *Proc Natl*  
578 *Acad Sci U S A* 2014; **111**: 17254–9.
- 579 40 Hill RJW, Innominato PF, Lévi F, Ballesta A. Optimizing circadian drug infusion  
580 schedules towards personalized cancer chronotherapy. *PLOS Comput Biol* 2020; **16**:  
581 e1007218.
- 582 41 Hacot S, Coute Y, Belin S, Albaret MA, Mertani HC, Sanchez J-C *et al.* Isolation of  
583 nucleoli. *Curr Protoc Cell Biol* 2010; **Chapter 3**: Unit3.36.
- 584 42 Poulard C, Jacquemetton J, Pham TH, Le Romancer M. Using proximity ligation assay  
585 to detect protein arginine methylation. *Methods* 2019.  
586 doi:10.1016/J.YMETH.2019.09.007.
- 587 43 Lausen B, Schumacher M. Maximally Selected Rank Statistics. *Biometrics* 1992; **48**:  
588 73–85.
- 589  
590

591

592

593 **FIGURE LEGENDS**

594 **Figure 1.** NLRP3 down-regulation impairs ATM-dependent IRIF formation and DNA damage  
595 signaling in response to DNA double strand breaks.

596 (A to D) HBEC3-KT transfected with control (siCTL) or NLRP3 siRNA (siNLRP3) were  
597 treated with IR (2 Gy). The number of nuclear  $\gamma$ H2AX (A), MDC1 (B), P-ATM (C), and 53BP1  
598 (D) IRIF were determined by immunofluorescence at indicated time points. IF of the 1 h time  
599 point is shown (x60). Hoechst (blue) was used to stain nuclei. Representative of four (A, C)  
600 and two independent experiments (B, D) ( $64 \leq n \leq 148$ ) Scale bars 10  $\mu$ m. (E) Mathematical  
601 modeling of ATM and NLRP3 interactions. Two hypotheses were investigated A) NLRP3  
602 enhances ATM activation, B) NLRP3 inhibits ATM deactivation.

603

604 **Figure 2.** NLRP3 is instrumental for optimal ATM activation.

605 (A) HBEC3-KT transfected with indicated siRNA were IR treated (10 Gy) and collected at  
606 different time points and P-KAP1 analyzed by immunoblotting. (B) HBEC3-KT control siRNA  
607 and NLRP3 siRNA were exposed to Eto (100  $\mu$ M) for indicated time points and P-KAP1 and  
608 P-p53 were analyzed by immunoblot. (C) Relative quantification of immunoblot of 3  
609 independent experiments as shown in (D). (E) Bone marrow-derived macrophages of wild type  
610 NLRP3 or NLRP3-depleted mice were treated with Eto 100  $\mu$ M over time and P-ATM and P-  
611 KAP1 were analyzed by immunoblotting (representative of 2 experiments). Data represent  
612 mean  $\pm$  SEM, \*\*\* P < 0.001, \*\*\*\* P < 0.0001, ns: not significant (unpaired t-test).

613

614 **Figure 3.** Expression of NLRP3 in NSCLC cell lines improves ATM activation after the  
615 induction of DNA DSBs.

616 A549 (**A** and **B**) or H292 (**C** and **D**) cells stably expressing a doxycycline-inducible NLRP3  
617 lentiviral vector (pSLIK NLRP3) induced or not with 0.5  $\mu\text{g}/\text{mL}$  doxycycline were irradiated  
618 with 2 Gy and P-ATM (**A** and **C**) and  $\gamma\text{H2AX}$  (**B** and **D**) IRIF assessed 1 h post-treatment. (**E**)  
619 H292 cells stably expressing the control or NLRP3 lentiviral vector were induced with  
620 doxycycline 24 h before being treated with etoposide over a time course of 16 h. KAP1 and p53  
621 phosphorylation was analyzed by immunoblot at the indicated time points. One representative  
622 experiment out of 3. \*\*\*\*  $P < 0.0001$ , \*\*\*  $P < 0.001$ , \*  $P < 0.05$  (unpaired t-test).

623

624 **Figure 4.** NLRP3 controls the DDR in an inflammasome-independent manner.

625 (**A**) HBEC3-KT control siRNA and caspase-1 siRNA (siCASP1) were treated with Eto 100  $\mu\text{M}$   
626 and H2AX phosphorylation was monitored by immunoblot. (**B**) HBEC3-KT control siRNA  
627 were treated with the pan caspase inhibitor z-VAD-fmk (50  $\mu\text{M}$ ) or the caspase-1 inhibitor z-  
628 YVAD-fmk (50  $\mu\text{M}$ ) 30 min before HU treatment (2 mM, 16 h) and H2AX phosphorylation  
629 was analyzed by immunoblotting. (**C**) HBEC3-KT transfected with control or NLRP3 siRNA  
630 were treated with IR 2 Gy or (**D**) HU 2 mM for the indicated times and IL-1 $\beta$  was quantified in  
631 cell supernatants using a Luminex assay. The line indicates the detection limit. (**E**) HBEC3-KT  
632 cells were treated with Eto 100  $\mu\text{M}$  over time and caspase-1 cleavage was analyzed by  
633 immunoblot. Actin was used as loading control. These data are from one representative  
634 experiment out of two independent experiments. n.d.: not detected

635

636 **Figure 5.** NLRP3 forms a complex with ATM.

637 (**A**) mcherry-NLRP3 and Flag-ATM co-immunoprecipitate in HeLa cells. Immunoprecipitates  
638 (IP) and input were analyzed by immunoblotting. (**B**) HeLa cells expressing Flag-NLRP3 were  
639 treated or not with Eto for indicated time points. Co-immunoprecipitation of endogenous ATM  
640 was analyzed by immunoblotting. (**C**) Different flag-tag NLRP3 domain constructs were

641 transfected in HeLa cells, and Flag-proteins were immunoprecipitated and pull-downed  
642 proteins were analyzed by immunoblotting. **(D)** Proximity Ligation Assay was performed in  
643 HBEC3-KT cells treated or not with Eto using anti-ATM and anti-NLRP3 (x40). Hoechst (blue)  
644 was used to stain nuclei. Scale bars 50  $\mu$ m Signal quantification is shown on the graph on the  
645 right panel. NT: not treated.

646

647 **Figure 6.** The absence of NLRP3 confers resistance to acute genotoxic stress.

648 **(A and B)** HBEC3-KT transfected with the indicated siRNA were treated with Eto and **(A)**  
649 caspase-3/7 activity was then measured by luminometry and **(B)** cell survival by cristal violet  
650 cytotoxicity test. \*\*\*\* P < 0.0001, \*\* P = 0.0046 (unpaired t-test). Results are representative of  
651 three experiments. **(C)** *NOXA* and *PUMA* expression were assessed in HBEC3-KT treated with  
652 Eto at the indicated time points by Q-RT-PCR relative to *HPRT1* expression. \*\*\*\* P < 0.0001,  
653 \*\* P = 0.0035 (multiple comparisons for two-way ANOVA). **(D)** *NOXA* expression was  
654 assessed by immunoblotting. Actin was used as a loading control. Representative of two  
655 independent experiments.

656

657 **Figure 7.** NLRP3 expression is reduced in human NSCLC compared to healthy tissue.

658 **(A)** Protein levels of the NLRP3 inflammasome components NLRP3, caspase-1 and ASC were  
659 assessed by immunoblotting and **(B)** relative *NLRP3* mRNA by Q-RT-PCR in HBEC3-KT cells  
660 and in a panel of NSCLC cell lines. Results are representative of more than three experiments.  
661 **(C)** Relative *NLRP3* mRNA levels were determined by Q-RT-PCR in a cohort of non-treated  
662 primary tumors from NSCLC patients (n = 20) and the corresponding normal lung tissues (n =  
663 10). Data represent mean  $\pm$  SEM; \*\*\* P < 0.001 (t-test). Kaplan-Meier plots of patients overall  
664 survival **(D)** and progression free interval **(E)** in TCGA-LUAD dataset according to NLRP3

665 expression levels; patients were stratified according to the cutoff obtained from maximally  
666 selected rank statistic.

667

668 **Supplementary Figure 1.** NLRP3 down-regulation impairs ATM-dependent IRIF formation.

669 **(A)** Immunoblot controlling the efficacy of the siRNA targeting NLRP3 (siNLRP3) against  
670 non-targeting siRNA (siCTL) of the HBEC3-KT irradiated cells. Actin was used as a loading  
671 control. **(B and C)** Representative pictures of HBEC3-KT cells transfected with control or  
672 NLRP3 siRNA and treated with 2 Gy for 1 h to assess MDC1 **(B)** or 53BP1 **(C)** foci formation  
673 was analyzed by IF. (x60), Hoechst (blue) was used to stain nuclei. Scale bars 10  $\mu$ m. **(D)**  
674 Scheme displaying the hypothesis used for mathematical modeling of ATM and NLRP3  
675 interactions showing the two hypotheses were investigated A) NLRP3 enhances ATM  
676 activation, B) NLRP3 inhibits ATM deactivation.

677

678 **Supplementary Figure 2.** ATM activity is impaired in the absence of NLRP3 in response to  
679 DNA damaging agents.

680 **(A)** HBEC3-KT siRNA-transfected cells were treated with 2 mM HU. At indicated time points,  
681 cells were lysed and protein extracts analyzed by immunoblotting for NLRP3,  $\gamma$ H2AX (S139),  
682 P-p53 (S15), P-KAP1 (S824). Actin was used as a loading control. **(B to D)** HBEC3-KT cells  
683 transfected with control or NLRP3 siRNA were treated with **(B)** 0.5  $\mu$ M etoposide for 4 h and  
684 P-ATM foci were quantified, and **(C)** 100  $\mu$ M Eto and mean fluorescence intensity was  
685 quantified in the nucleus, **(D)** 0.5  $\mu$ M etoposide for 4 h and  $\gamma$ H2AX foci quantified. (x60),  
686 Hoechst (blue) was used to stain nuclei. Data represent mean  $\pm$  SEM; \*\*\* 0.001 < P (unpaired  
687 t-test). Scale bar 10  $\mu$ m **(E)** ROS measurement was performed on HBEC3-KT cells transfected  
688 with control or NLRP3 siRNA using DCFDA probe in presence or in absence of 5  $\mu$ M ATMi  
689 KU5593. One representative experiment out of 3.

690

691 **Supplementary Figure 3.** NLRP3 re-expression in tumoral cell lines facilitates ATM-  
692 dependent DNA damage signaling.

693 A549 (**A** and **B**) or H292 (**C** and **D**) stably expressing a doxycycline-inducible NLRP3 lentiviral  
694 vector treated or not with 0.5  $\mu$ M of doxycycline were irradiated with 2 Gy for 1 h.

695 Representative pictures of P-ATM (**A** and **C**) and  $\gamma$ H2AX (**B** and **D**) IF staining that was  
696 quantified in Figure 3 A to D. (x60), Hoechst (blue) was used to stain nuclei. Scale bars 10  $\mu$ m.

697 (**E**) H520 cells stably expressing the NLRP3 or CTL vector were treated with 0.5  $\mu$ g/mL of  
698 doxycycline 24 h before irradiation with 6 Gy. At indicated time points, cells were lysed and

699 protein extracts analyzed for NLRP3,  $\gamma$ H2AX (S139), P-KAP1 and KAP1 by immunoblotting.

700 Actin was used as a protein loading control.

701

702 **Supplementary Figure 4.** NLRP3 is localized in the cell cytosol and nucleus, but most  
703 NLRP3/ATM complexes are present in the cell cytosol.

704 (**A**) HBEC3-KT untreated (0) or irradiated (2 Gy) were separated and proteins from the  
705 cytosolic (C) and nuclear (N) fractions were analyzed by immunoblot. Tubulin was used as a

706 marker of the cytosolic fraction and fibrillarin of the nuclear fraction. T is total lysate. (**B**)

707 Confocal images illustrating the cellular localization of the different NLRP3 domains

708 transfected in HeLa cells (x63). Hoechst (blue) was used to stain nuclei. (**C**) NLRP3 is detected

709 in the cytosol and the nucleus compartment in live confocal image of mCherry-NLRP3

710 transfected in H292 cells. (**D**) Proximity Ligation Assay in HeLa cells transfected with an empty

711 vector or a NLRP3-expressing vector using anti-ATM and anti-NLRP3 antibodies (x40).

712 Hoechst (blue) was used to stain nuclei.

713

714 **Supplementary Figure 5.** NLRP3 silencing decreases nuclear ATM.

715 (A and B) HBEC3-KT sh control cells or knocked down for NLRP3 were left untreated (A) or  
716 irradiated at 2 Gy for 1 h (B). Total ATM was stained for immunofluorescence and the mean  
717 fluorescent intensity was quantified. Results are representative of two independent experiments  
718 (x60). Hoechst (blue) was used to stain nuclei. Scale bar 10  $\mu$ m.

719

720 **Supplementary Figure 6.** NLRP3 does not control the extrinsic apoptosis pathway.

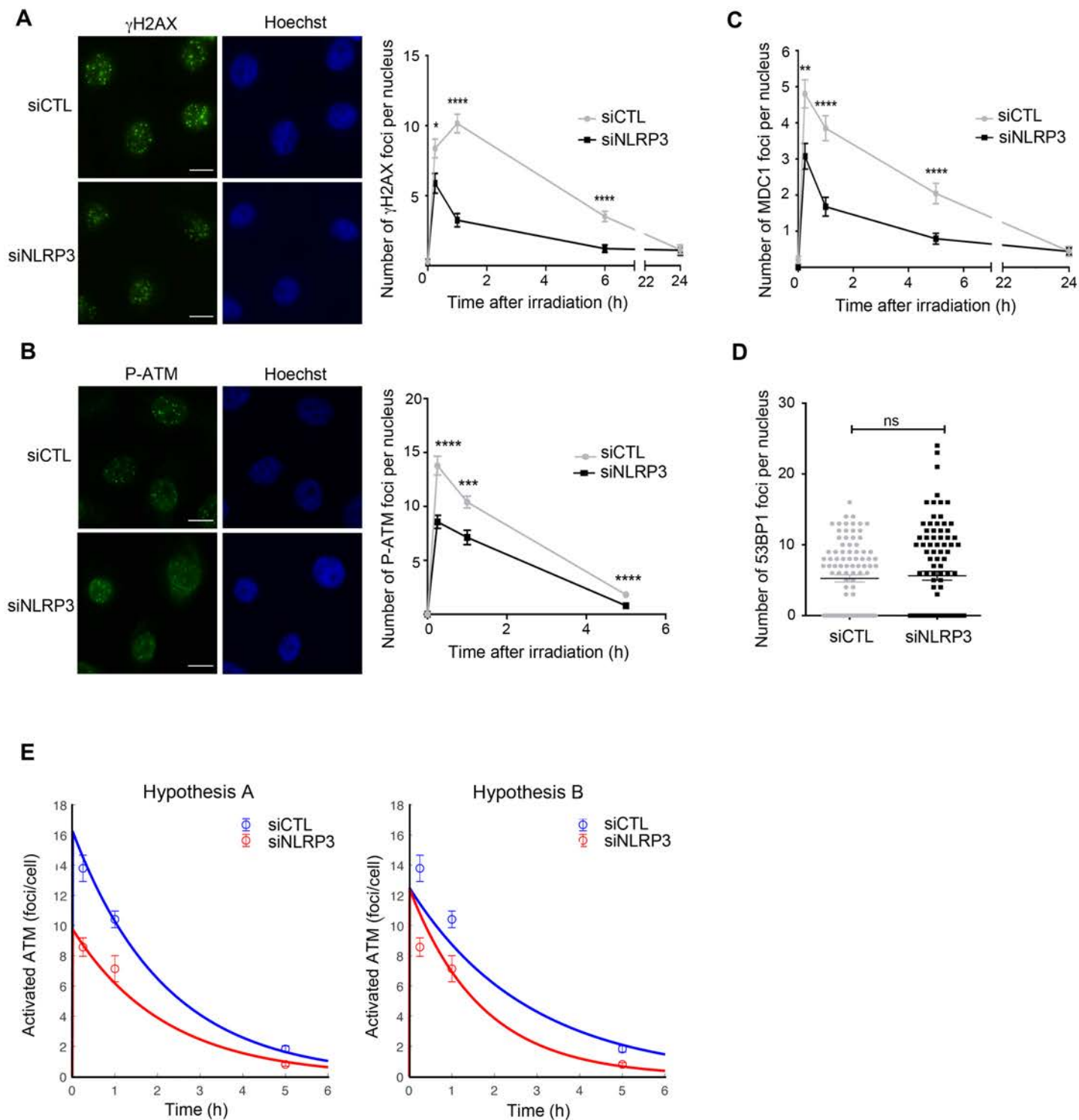
721 (A) HBEC3-KT cells transfected with control or NLRP3 siRNA were treated with Trail 200  
722 ng/mL and MG132 1 mM for 12 h to induce death receptor-mediated apoptosis. Data represent  
723 mean  $\pm$  SEM; ns: not significant (t-test). (B) Model of resistance to genotoxic stress caused by  
724 reduced NLRP3 expression. DNA DSBs activate the ATM kinase which phosphorylates many  
725 protein substrates involved in the control of the outcome to genotoxic stress. Down-regulation  
726 of NLRP3 impairs ATM activation resulting in decreased levels of phosphorylation of several  
727 ATM substrates, including p53, thus promoting cell survival.

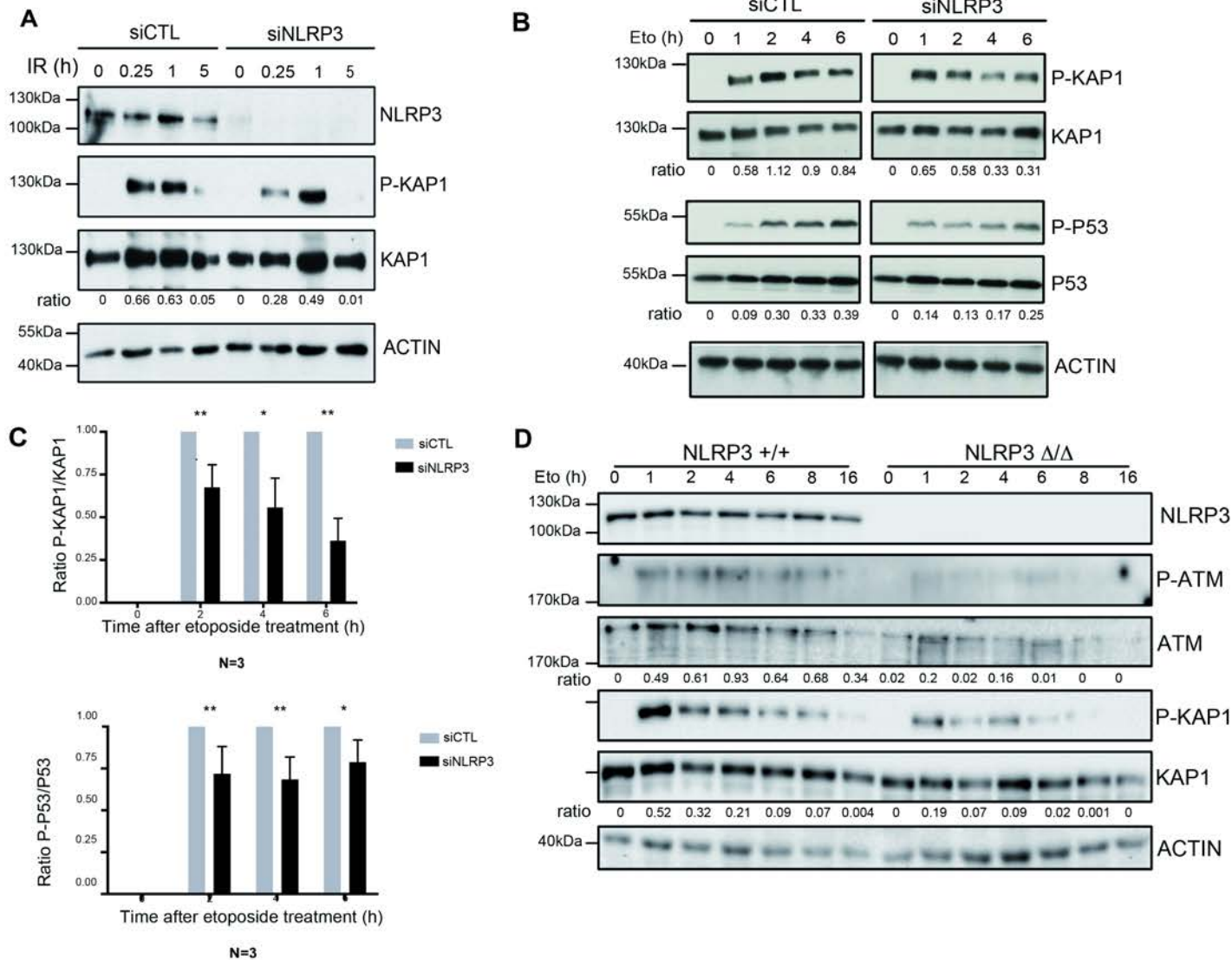
728

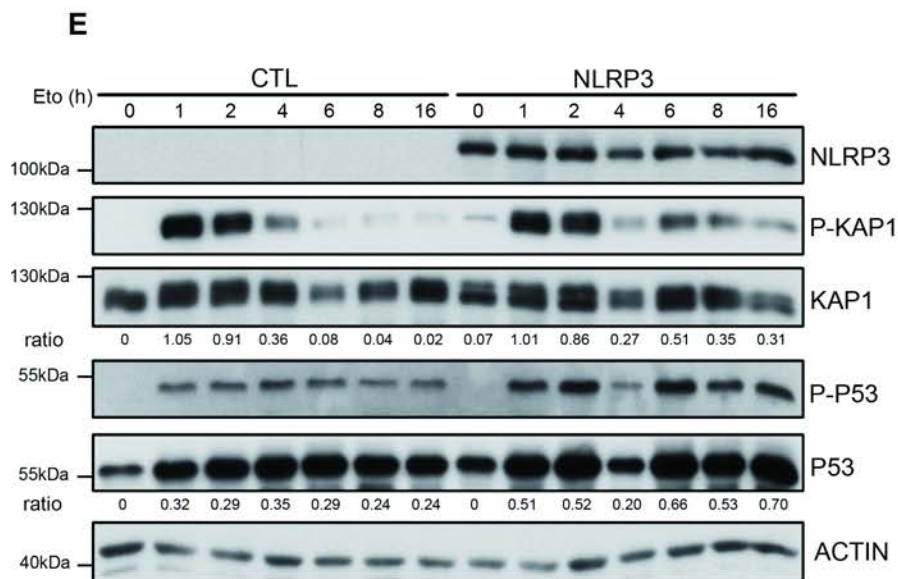
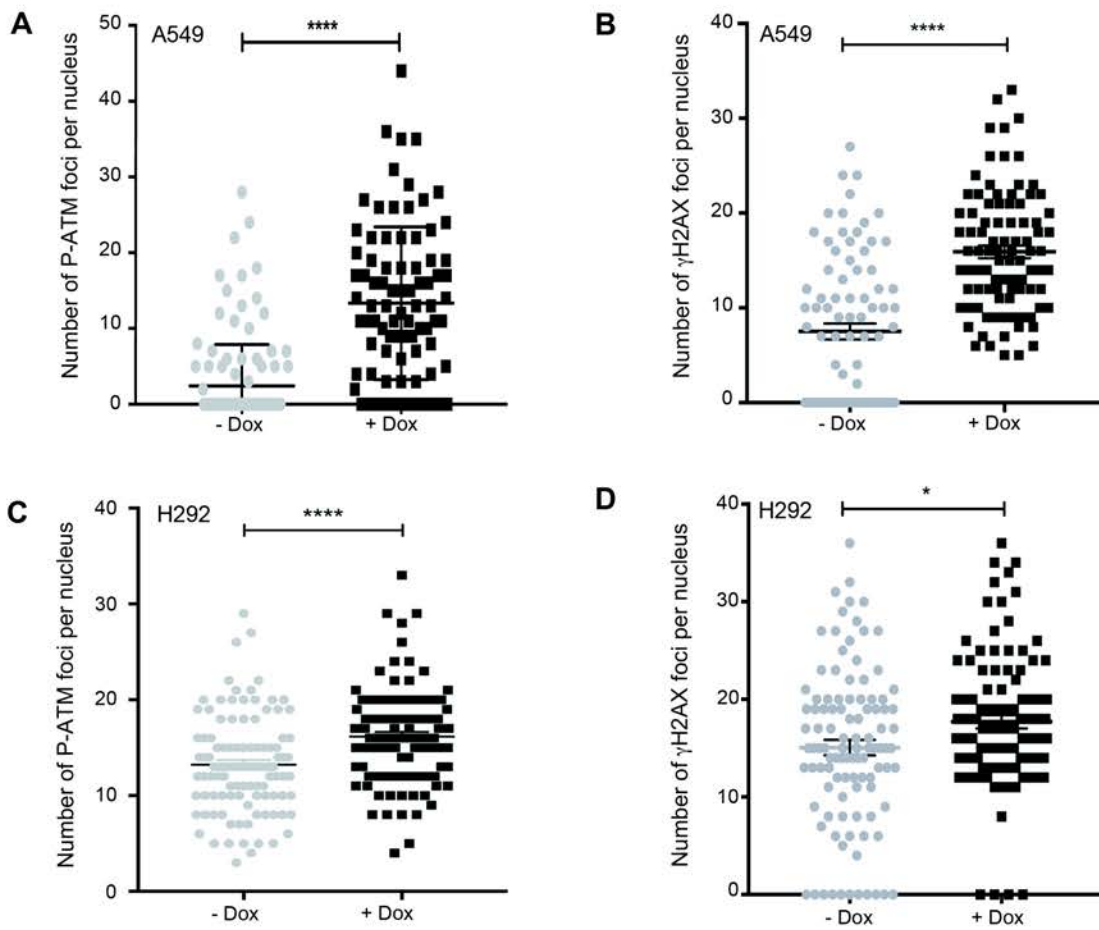
729 **Supplementary Figure 7.** NLRP3 expression is reduced in human NSCLC compared to non-  
730 tumoral cells.

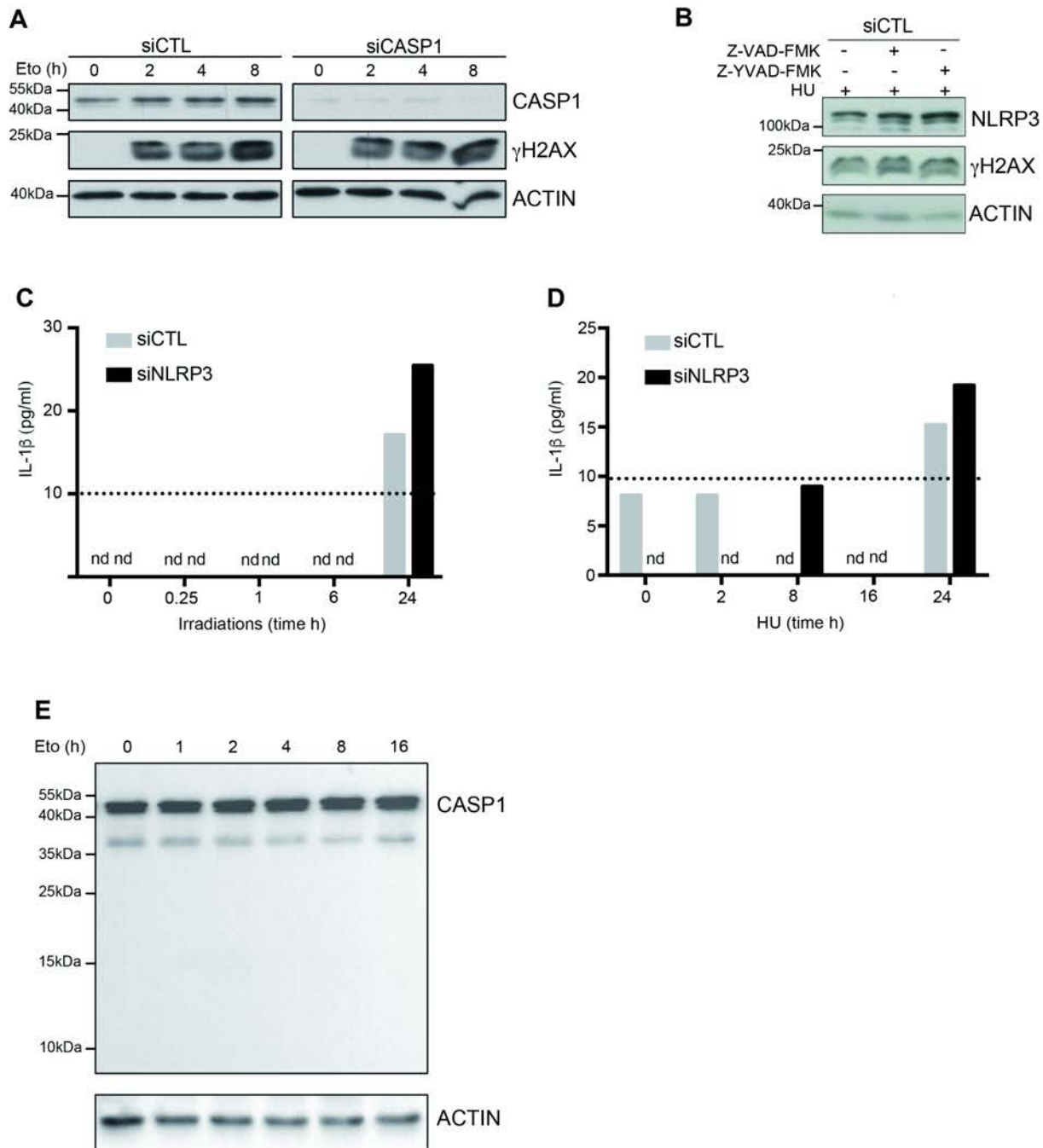
731 (A) NLRP3 inflammasome components, namely NLRP3, caspase-1 and ASC were assessed by  
732 immunoblotting in NSCLC cell lines. GAPDH was used as a protein loading control. (B)  
733 Anchorage-independent growth ability was assessed in HBEC3-KT cell lines.

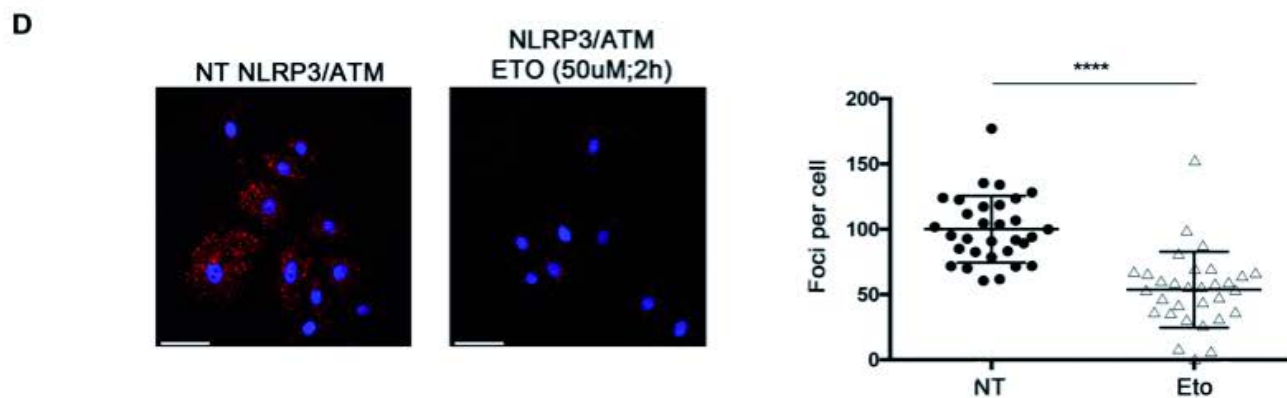
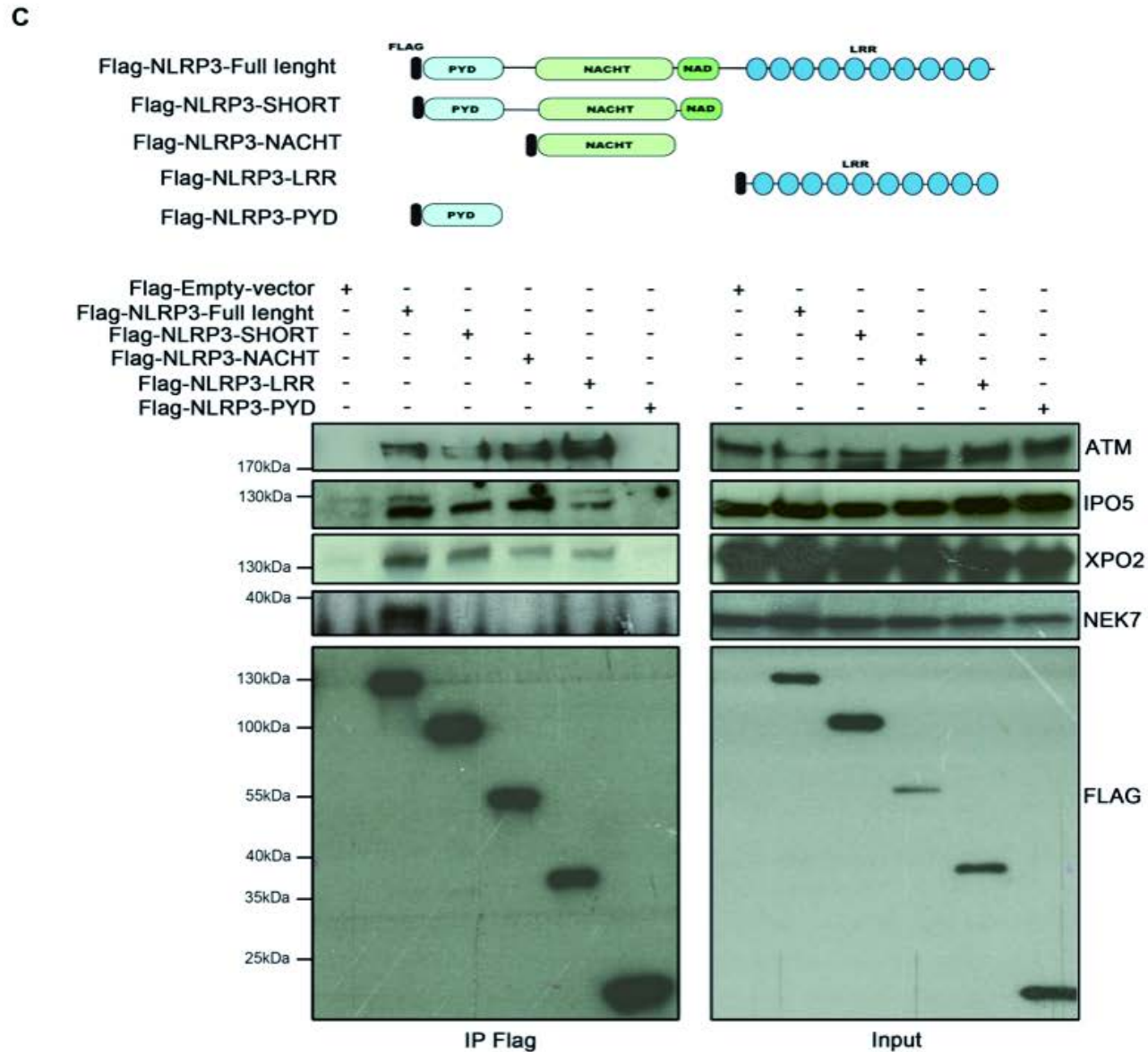
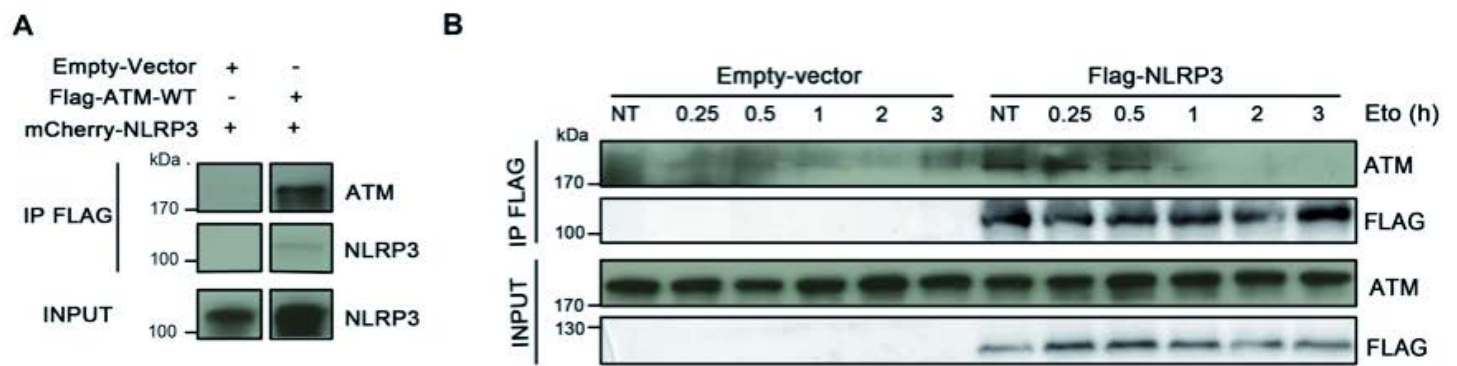
734

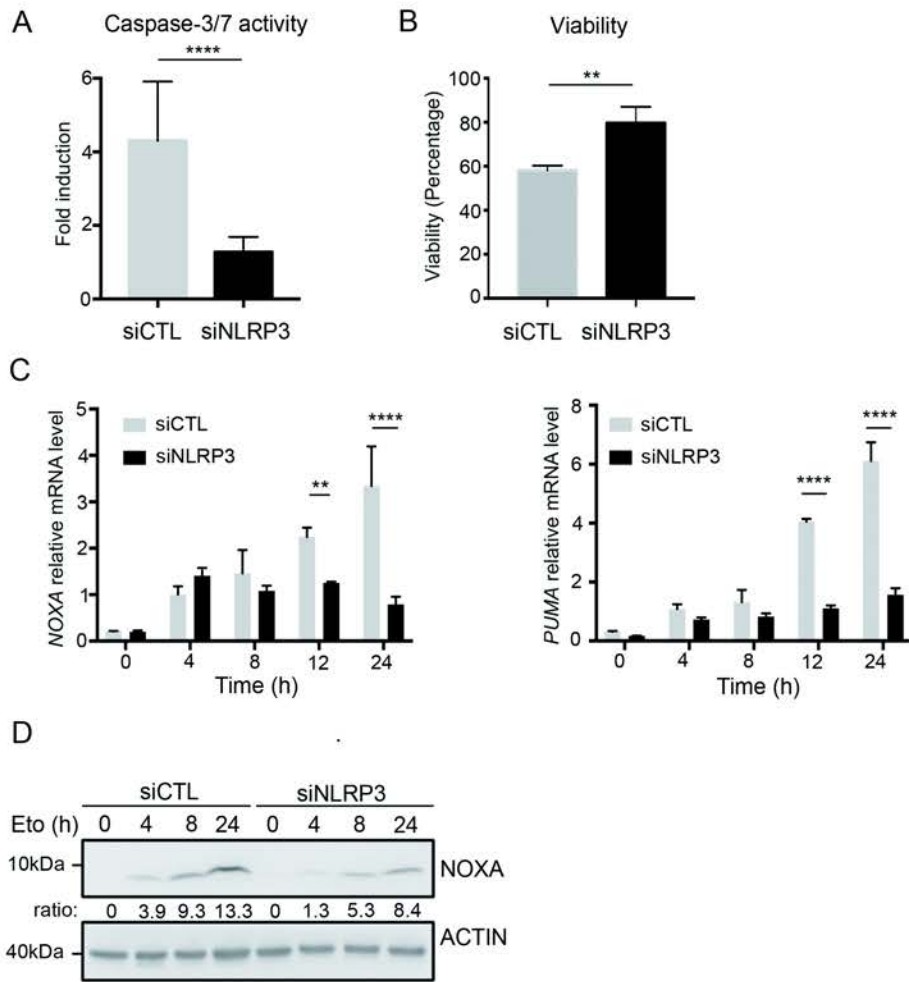


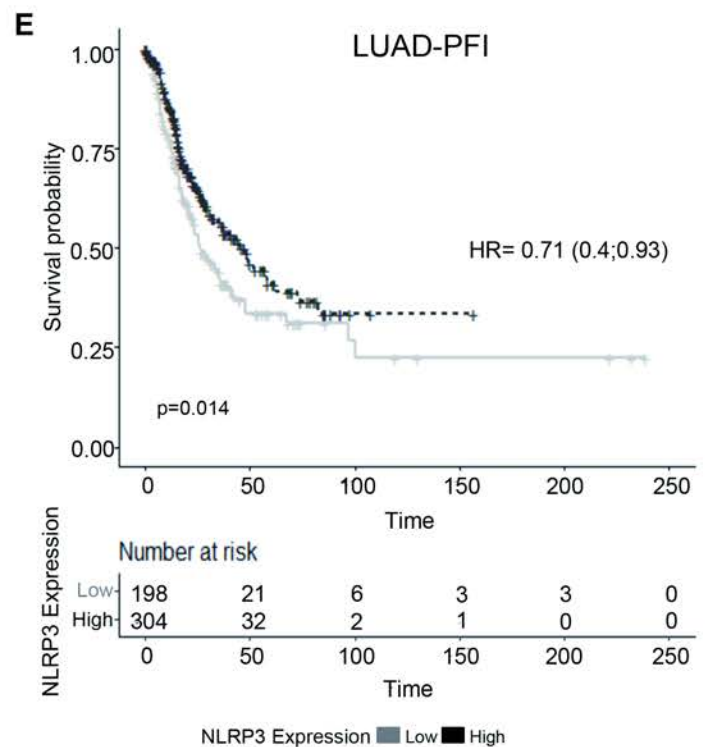
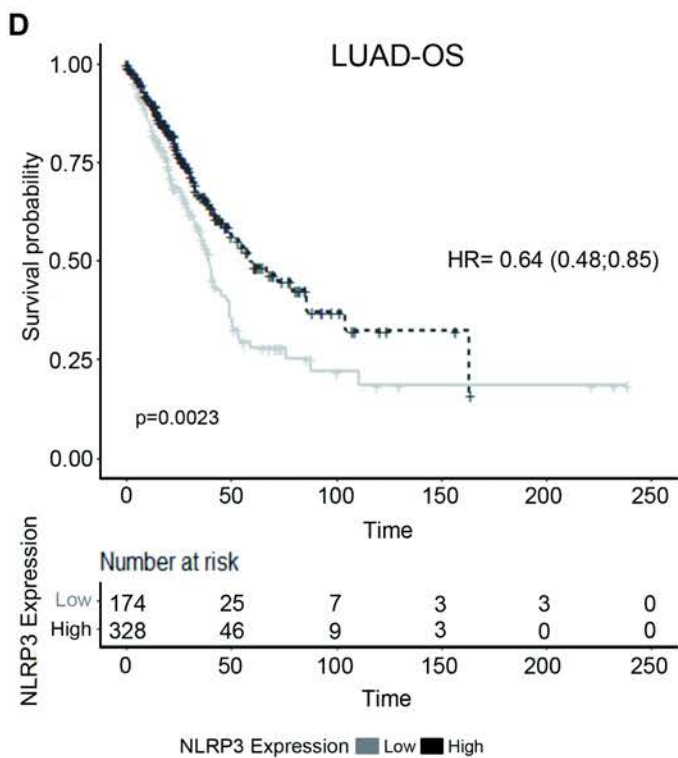
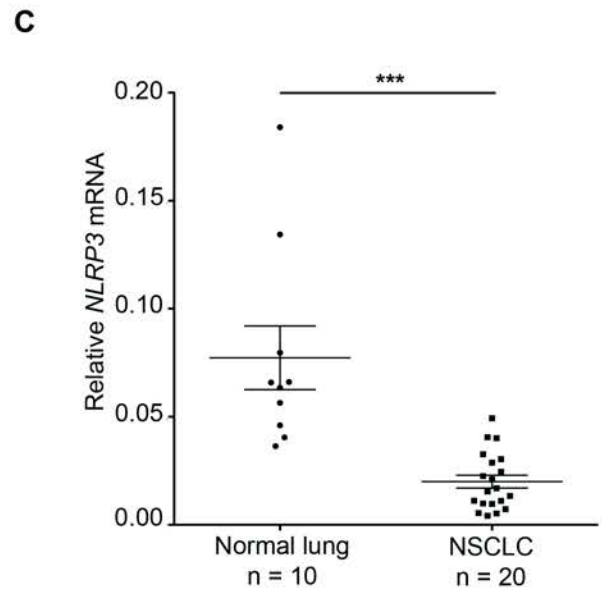
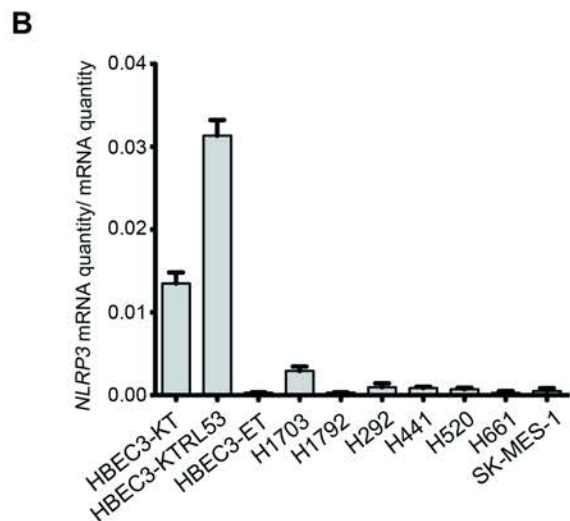
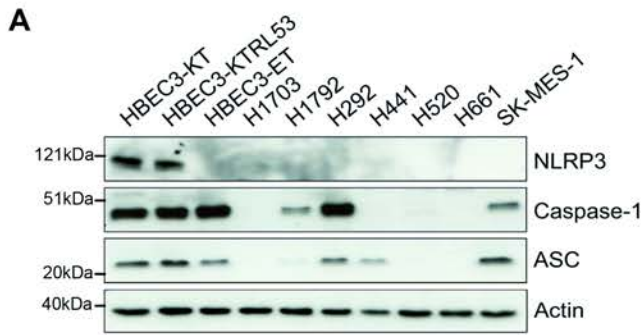


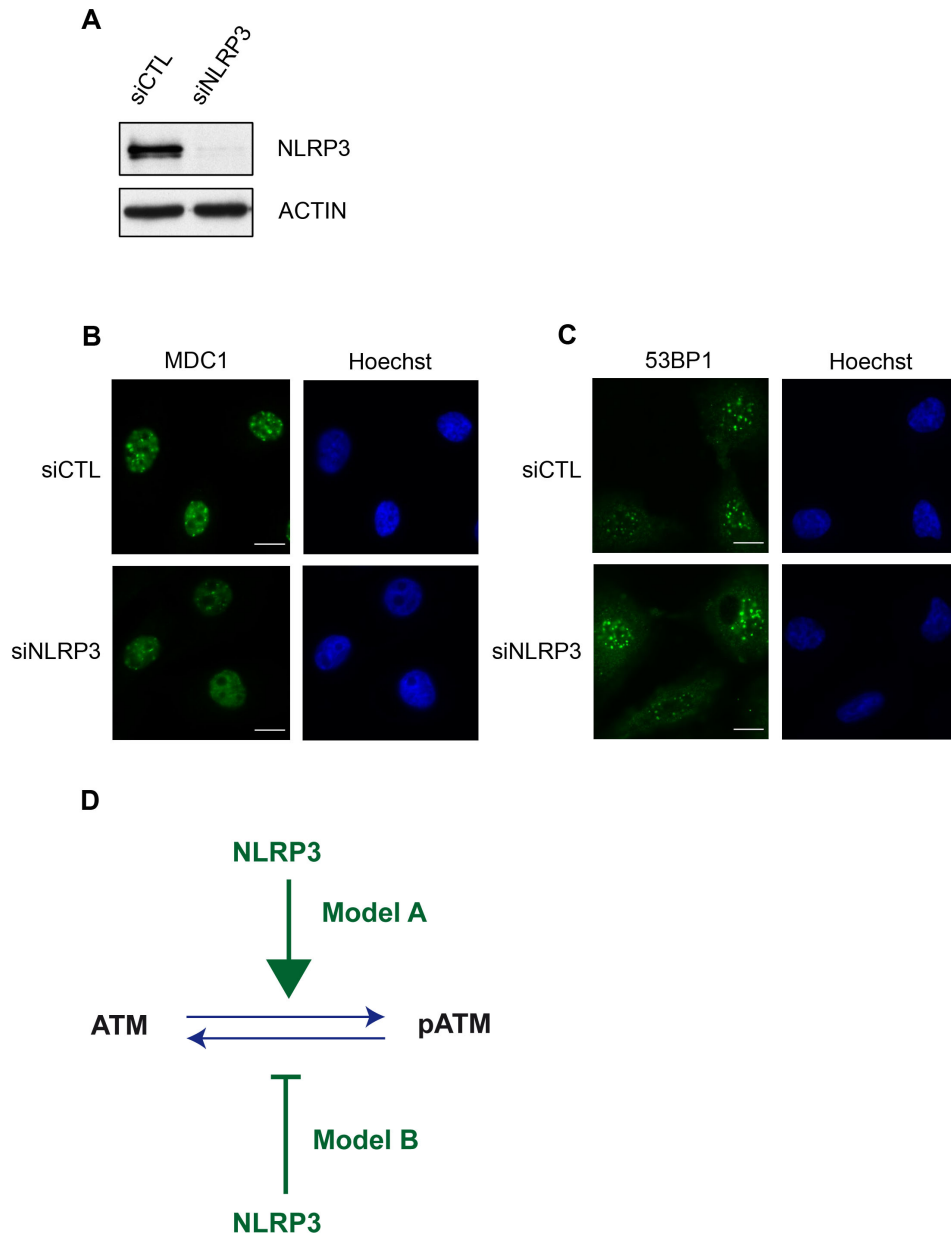


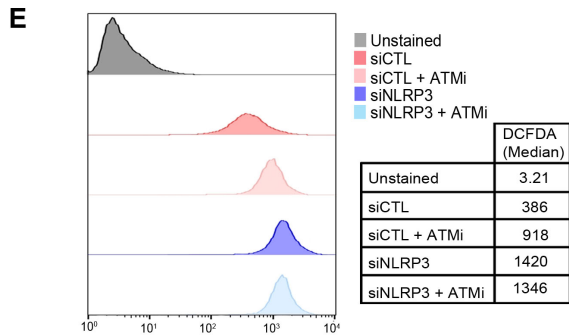
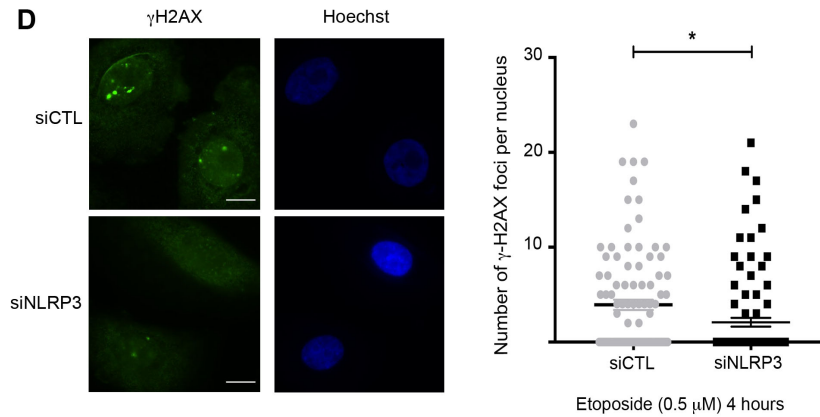
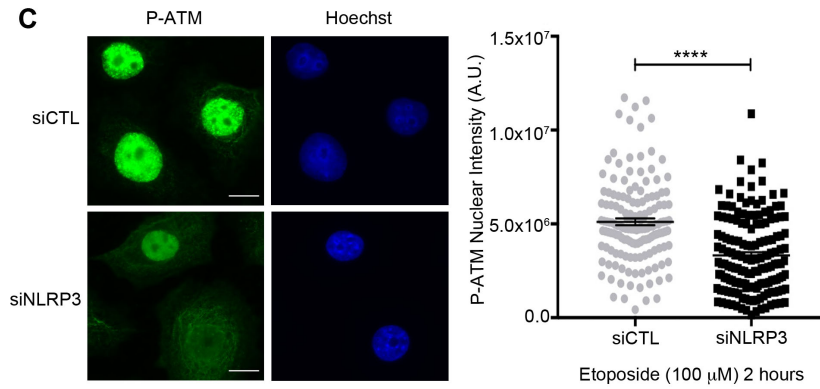
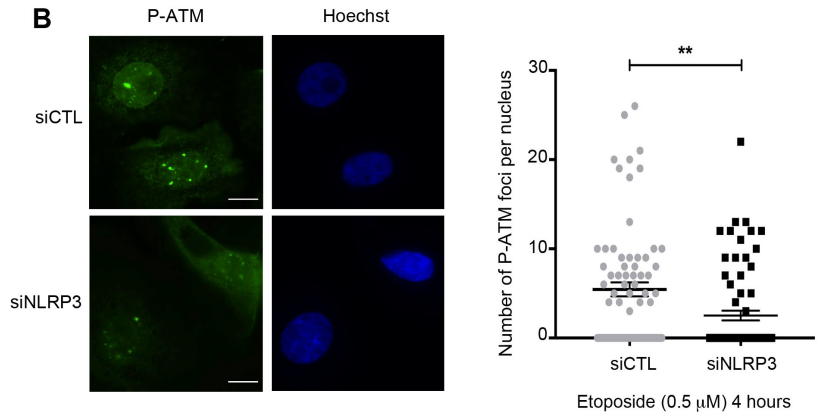
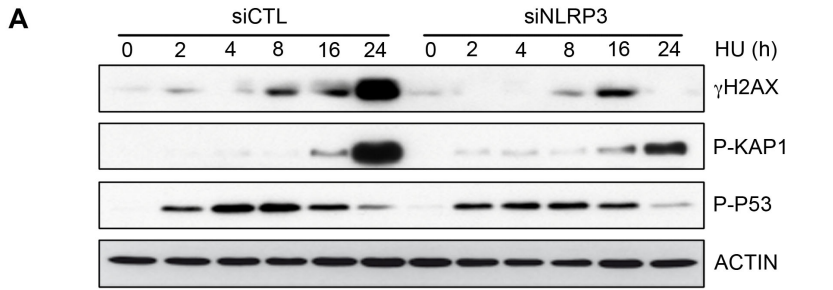




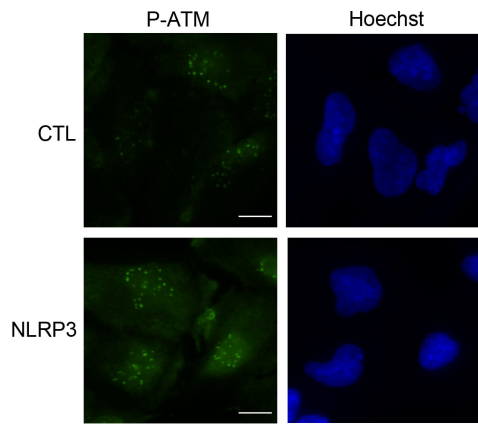




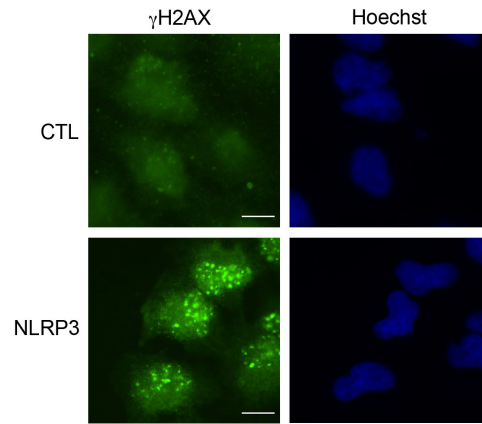




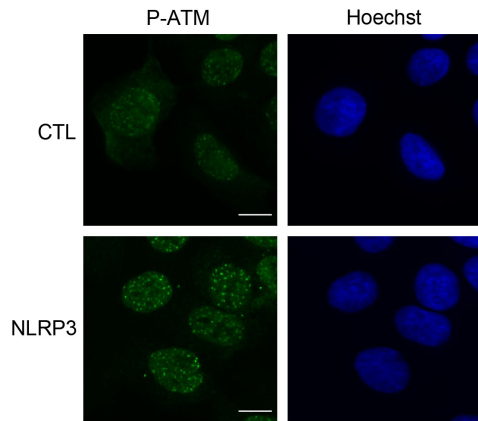
**A** A549



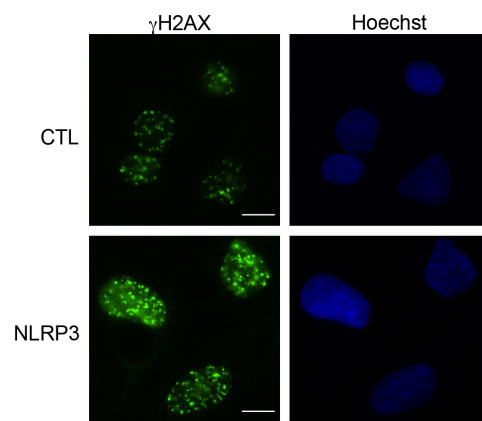
**B** A549



**C** H292



**D** H292



**E**

